# Malaysia Airlines Flight MH370: A Modeling and Simulation Study of Airplane Crash and Water Landing

Goong Chen[1], Cong Gu[2], Philip J. Morris[3], Eric G. Paterson[4], Alexey Sergeev[5], Yi-Ching Wang[6], and Tomasz Wierzbicki[7]

1: Goong Chen is professor of mathematics at Texas A&M University (TAMU) and Texas A&M University at Qatar (TAMUQ). He is also a member of the Institute for Quantum Science and Engineering at TAMU. His email address is gchen@math.tamu.edu.
2: Cong Gu is a Ph.D. student in the mathematics department of TAMU. His email address is gucong@math.tamu.edu.
3: Philip J. Morris is Boeing/A.D. Welliver Professor of Aerospace Engineering at The Pennsylvania State University. His email address is pjm@psu.edu.
4: Eric G. Paterson is Rolls Royce Commonwealth Professor of Marine Propulsion and department head of Aerospace and Ocean Engineering at Virginia Tech. His email address is egp@vt.edu.
5: Alexey Sergeev is postdoctoral fellow of mathematics at TAMU and TAMUQ. His email address is asergeev@asergeev.com.
6. Yi-Ching Wang is a Ph.D. student in the mathematics department of TAMU. Her email address is ycwang@math.tamu.edu.
7. Tomasz Wierzbicki is professor of applied mechanics and Director of Impact and Crashworthiness Laboratory at MIT. His email address is wierz@mit.edu.

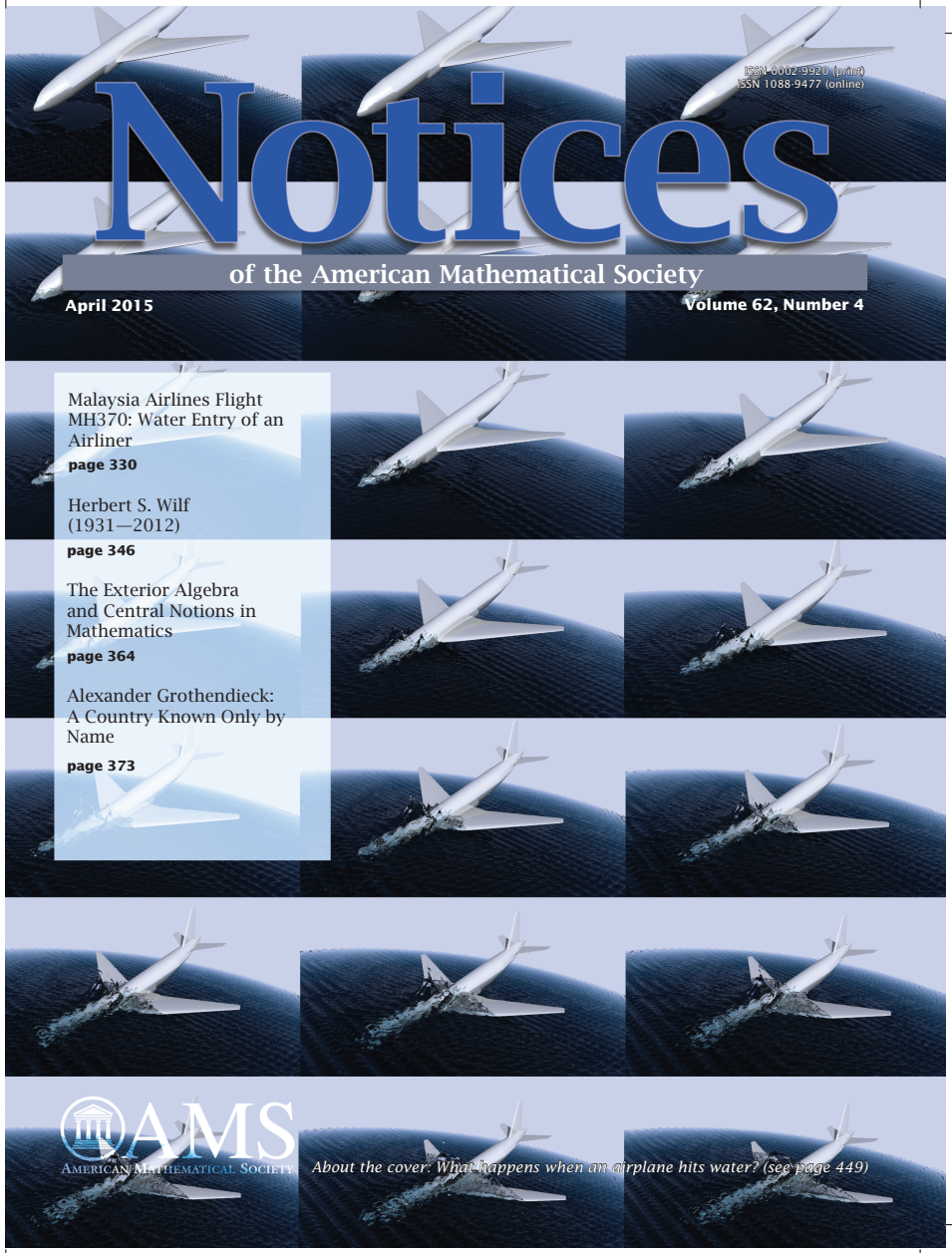
Notices
of the American Mathematical Society
April 2015
Volume 62, Number 4
ISSN 0002-9920 (print)
ISSN 1088-9477 (online)
Malaysia Airlines Flight MH370: Water Entry of an Airliner
page 330
Herbert S. Wilf (1931—2012)
page 346
The Exterior Algebra and Central Notions in Mathematics
page 364
Alexander Grothendieck: A Country Known Only by Name
page 373
AMS
American Mathematical Society
About the cover: What happens when an airplane hits water? (see page 449)

# 1 Introduction

On March 8, 2014 Malaysia Airlines Flight MH370 disappeared less than an hour after take-off on a flight from Kuala Lumpur to Beijing. The Boeing 777-200ER carried 12 crew members and 227 passengers. On March 24 the Malaysian Prime Minister announced that “It is therefore with deep sadness and regret that I must inform you that ... Flight MH370 ended in the Southern Indian Ocean.” Though the exact fate of Flight MH370 remains undetermined, the available evidence indicates a crash of the airliner into the ocean. However, disturbing as this is, not all emergency water landings, referred to as “ditching” when they are controlled, end in tragedy. In the “Miracle on the Hudson”, Capt. Chelsey B. “Sully” Sullenberger and his crew successfully ditched US Airways Flight 1549, an Airbus A320-200, in the Hudson River after a loss of power due a bird strike on take-off from La Guardia Airport. There was no loss of life.

Malaysia Prime Minister Perdana Menteri


March 24 2014
"It is therefore with deep sadness and regret that I must inform you that ... Flight MH370 ended in the Southern Indian Ocean."

**Figure 1:** US Airways Flight 1549 in the Hudson River.

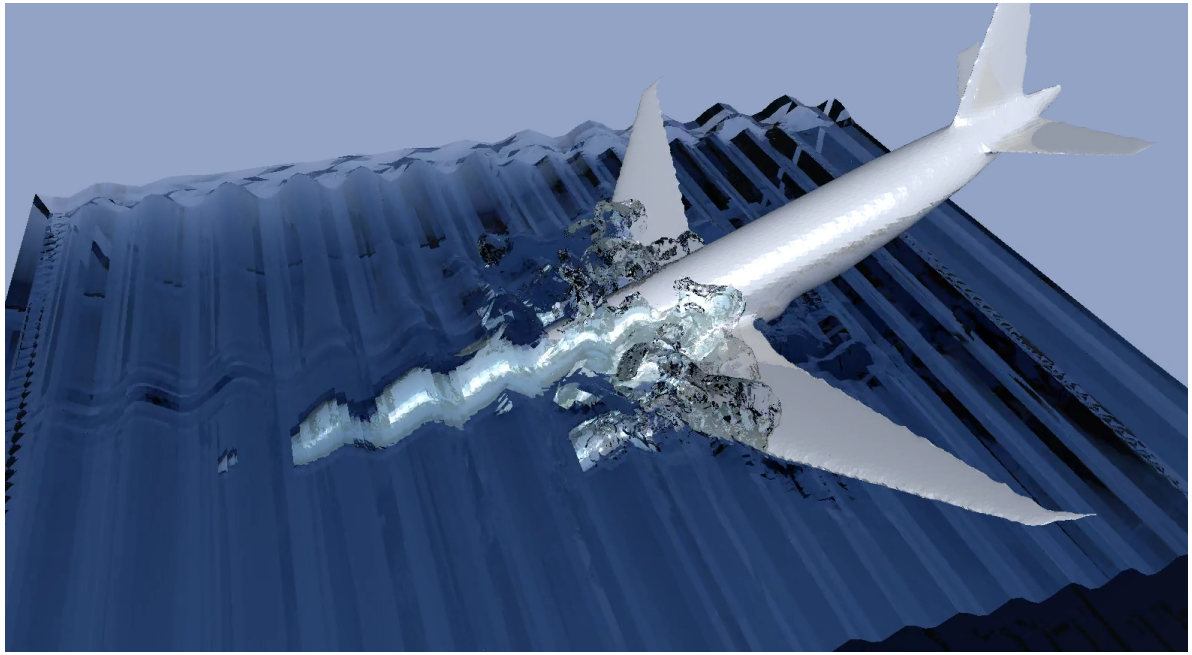

**Figure 2:** The aircraft is a Boeing 777 model flying into ocean at the speed of 70m/sec, with pitch angle = -20°, at time t=0.36 sec. A volume-of-fluid (VOF) scheme in OpenFOAM ( [1] ) is used to simulate the two-phase flow for the fluid-aircraft body interaction. Please also use the link `https://www.dropbox.com/s/pbjhrovlqrqiizm/smooth-cin40.avi` to view the corresponding video animation of the dynamic motion.

Figure 2 and the accompanying video animation show our "representation" of a commercial airliner (a Boeing 777 model) falling into the ocean. (See our commentary in Box 1 of Section 2). Such simulations can help to understand the physical mechanisms at work and also to improve passenger safety. But these are very challenging simulations that require the cooperation of engineers, mathematicians and computational scientists. Any scientific investigation of the mishap, apart from human factors of foul play and conspiracy, appears mostly of an *engineering nature*, such as machine and instrumentation breakdown, midair explosion, weather, navigation, etc. But this should not prevent mathematicians' curiosity from entering the fray to also add and contribute something valuable, regarding this investigation and recovery effort. The fact is, mathematics is closely interwined with engineering, and is not detached from the "real world" as some people may think.

An article articulating how the radar signal backtracking made by the British company Inmarsat works was published in SIAM News in [2], where John Zweck of the Math Dept of the University of Texas - Dallas argued in support of Inmarsat by using the Doppler frequency shift, time and locations of ping, trigonometry and other mathematical methods and MATLAB® software. Nevertheless, Inmarsat's radar tracking methodology and data analysis have not yet convinced everybody that they are ironclad; see some counter arguments by David Finkleman in [3], for example. (Dr. Finkleman is Director of Studies and Analysis, and Senior Scientist, North American Aerospace Defense Command and U.S. Space Command, at Peterson Air Force Base, Colorado.)

In this article, we provide a discussion of this air incident, from a mathematical as well as interdisciplinary perspective. We show how computational mathematics and mechanics can help us understand the physical nature of an aircraft emergency water landing, how to model and compute it, and how this knowledge is helping safe civil aviation and other aerospace related undertakings. Our work here essentially constitutes *flight simulations*, except that real-world flight simulators do not usually simulate the underwater situation of an aircraft.

The problem under consideration is *dynamic* in nature and is best viewed with the aid of *video animation*. We encourage the reader to see such animations through the various URLs provided in the article by pasting and then clicking them, using the online version of the paper in the *Notices* [4].

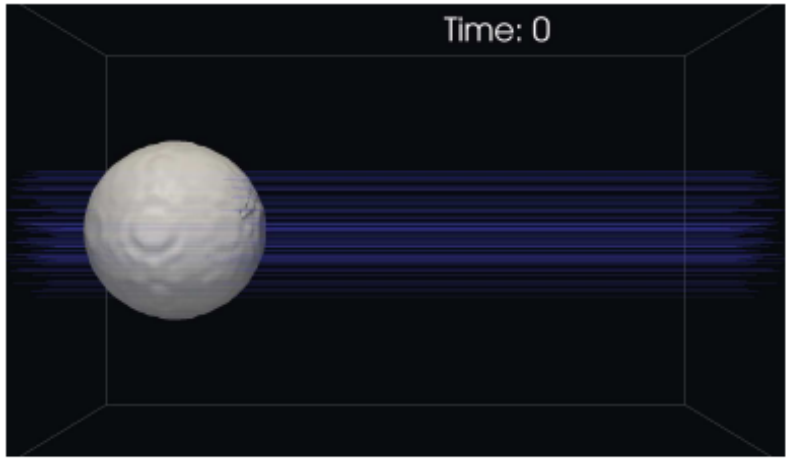


(a)

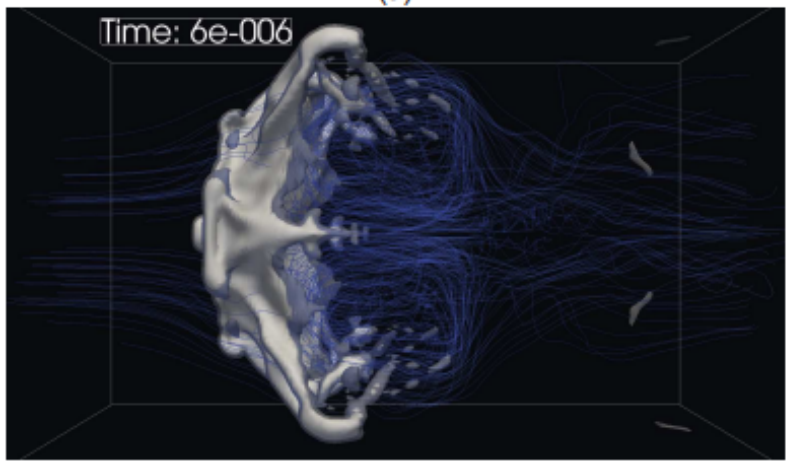


(b)

Breakup of spray moving in air with speed 200 m/sec.
(a) The droplet at $t = 0$ is nearly spherical, with diameter (approx.) 0.075 mm;
(b) Breakup of the spray at $t = 6 \times 10^{-6}$ sec.

**Figure 3:** `http://www.dimensionality.info/temp/multiphase/breakup/g.avi`.

## 2 The Water Entry Problem Revisited

The *water entry problem* is a classical problem in applied mathematics and fluid dynamics. It considers the dynamic motion of an object upon its entry into the water. The problem was motivated by several applications: the landing of a hydroplane, the entry into water of a rocket or the Apollo module returning from space and the ditching or crashing of aircraft.

# High Platform Diving (10 m, Fu Mingxia)

List of World Most Suicide Sites

(1) Golden Gate Bridge (more than 3000 since 1937)

(2) Nanjing Yangtze River Bridge (more than 2000, 1968 $\sim$ 2006)

(3) Prince Edward Viaduct (more than 492 before barrier installed)

A major contribution to this field was made by the celebrated applied mathematician and fluid dynamicist Theodore von Karman (1881-1963). He developed the idea of "added mass" (a mass of the fluid that is co-moving with the body) to study the problem [5]; see Figure 4. Von Karman inferred that the impact force on the body is related to the instantaneous change of total momentum of the body with its own mass but with an extra mass augmented by the "added mass" of the fluid around the submerged portion of the body. That is,

$$\frac{d}{dt}\left[(M+m(t))\dot{\zeta}(t)\right] = Mg - F_B - F_C - F_D \qquad \text{(cf. [6, eq.(2.3)])} \tag{0.1}$$

where $M$ =mass of the projectile, $m(t)$ = "added mass",
$F_B$ = buoyancy force, $F_C$ = capillary force,
$F_D$ = steady-state drag force, and
$\zeta(t)$ = depth of penetration into fluid.

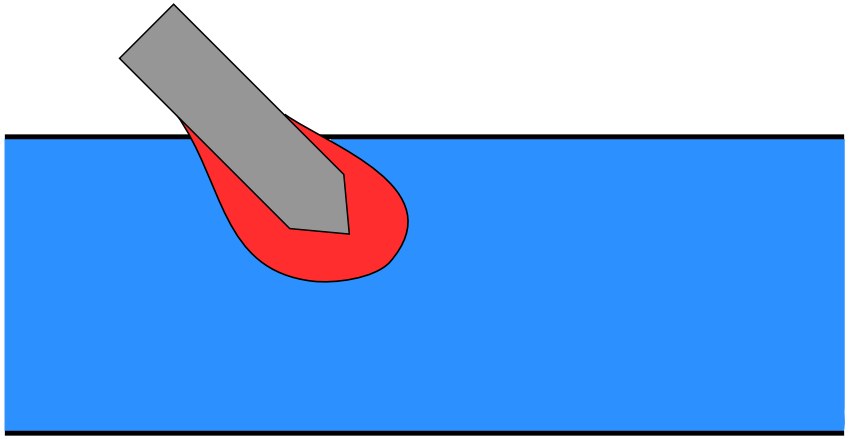

**Figure 4:** Von Karman's idea of "added mass" for the water entry problem, which is an idealization and simplification. Here the red region represent "added mass". This is the mass moving together with the mass of the wedge projectile. The portion of the (red) added mass lying above the still water surface is called the "pile up".

We note that the precise value of added mass $m(t)$ is not known. For small time or submerged depth upon entry of the body into the water, von Karman estimated the added mass to be half that of a flat plate with the same area as the instantaneous *still* water-plane of the body. Wagner [7] further improved von Karman's work by including the effect of the *pile up* of the water and by associating the added mass with the *wetted* water-plane. Further work such as [8] took account of the submerged geometry for the estimation of the added mass. The analysis and results from these simple approaches are found to compare favorably with experiments for simple geometries such as a wedge or a cone. They also helped the designs of air-to-subsea anti-submarine missiles, for example.

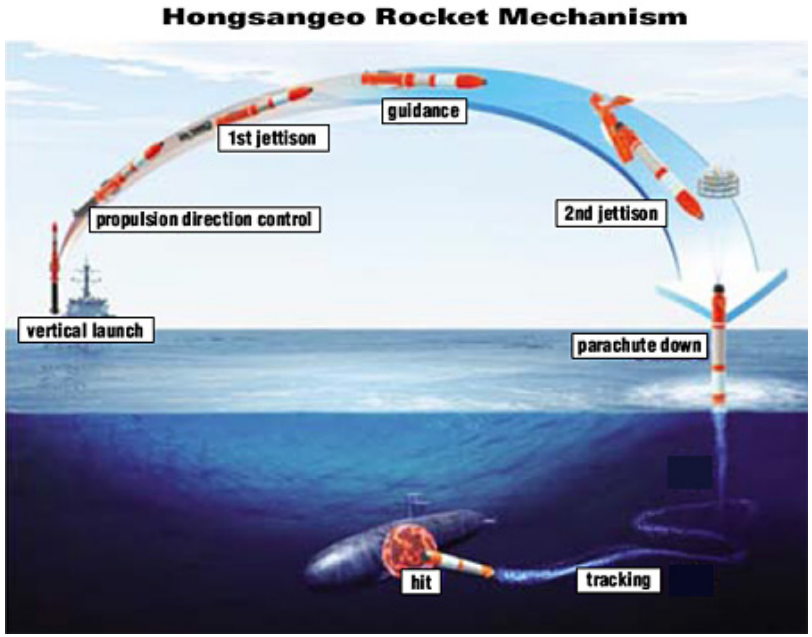
Hongsangeo Rocket Mechanism
guidance
1st jettison
propulsion direction control
2nd jettison
vertical launch
parachute down
hit
tracking

On the mathematical side, papers studying the water entry problem for a two-dimensional (2D) wedge were written by Shiffman and Spencer [9] for a normal incidence problem, and by Garabedian [10] for oblique incidence, for example. These papers treated the case of 2D incompressible, irrotational, inviscid flow by complex variables and potential theory techniques and offered rigorous analysis.
A comprehensive survey of water entry problems (up to the year 2011) can be found in [6], where 476 references are listed.

The contributions made by von Karman, Wagner, and others were truly remarkable, and they continue to be used today. However, the physics of water-entry is far more complex to model than the idea of "added mass" alone. In reality, there are several phases of water entry that have been observed in experiments [11]: (1) cavity-opening and jet splashing; (2) cavity-closing and formation of an air pocket; and (3) cavity-detachment and cavitation; see Figure 5. A good way to capture the rich physics is through state-of-the-art *computational fluid dynamics (CFD)*.

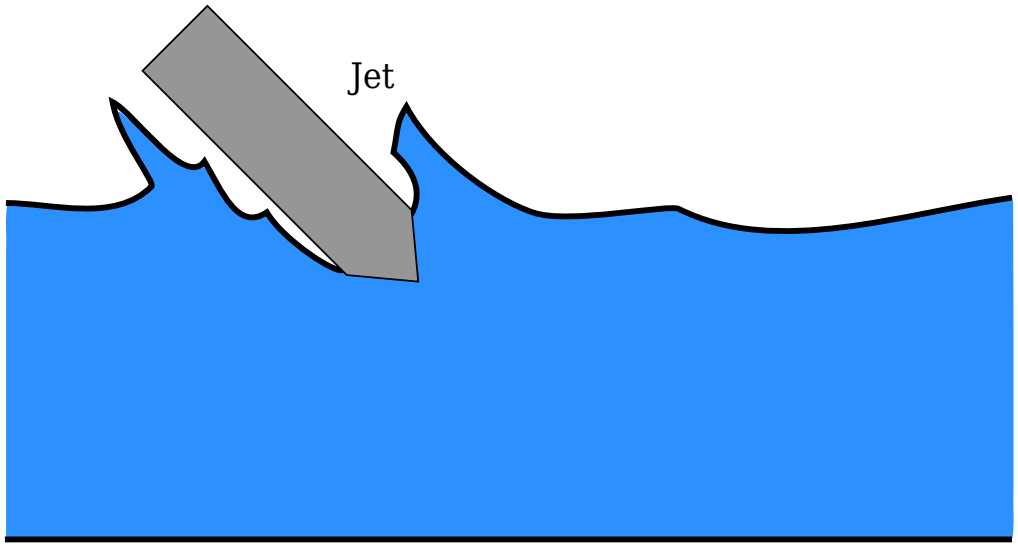


**(a)**

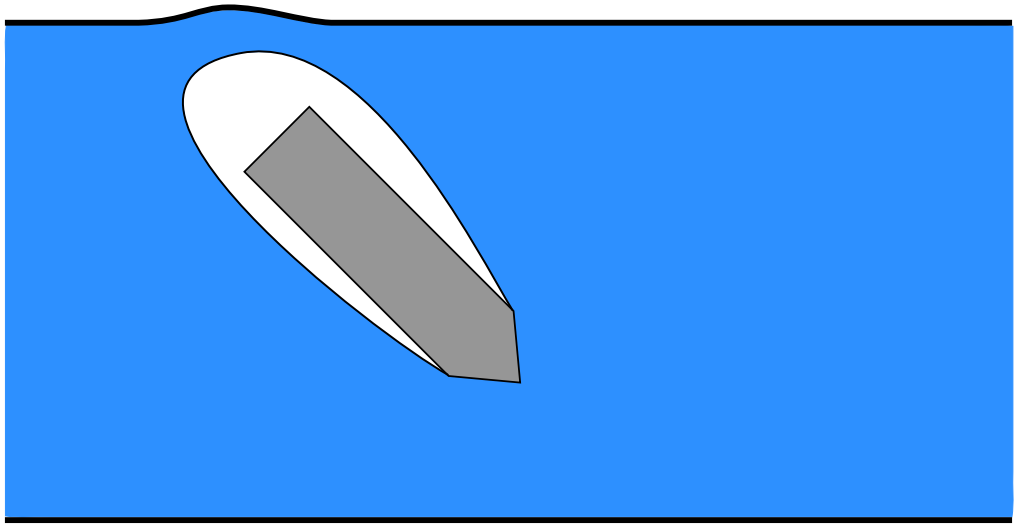

**(b)**

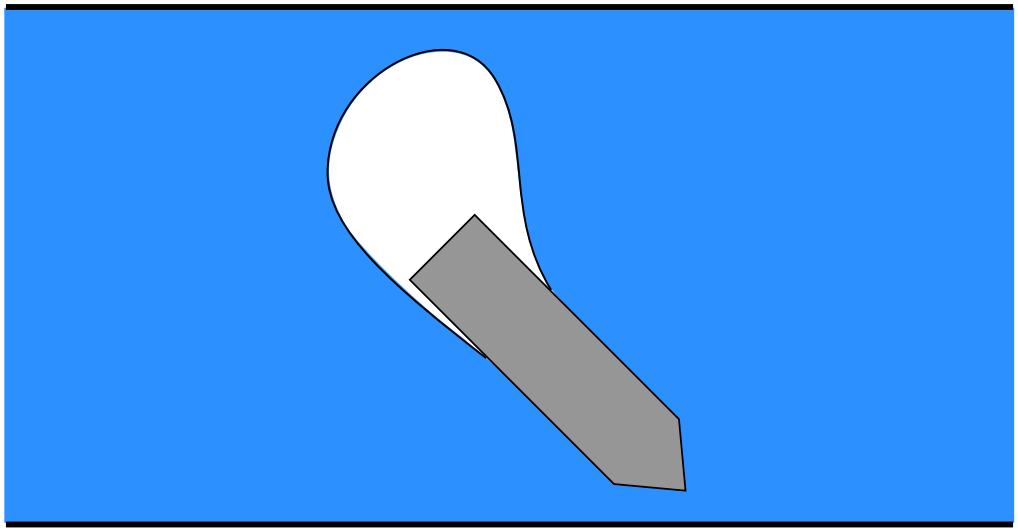

**(c)**

**Figure 5:** The several phases of a projectile entering water according to Mackey [11]: (1) a cavity of air opens; (2) a cavity of air pocket encloses the projectile when it is totally submerged; and (3) the cavity begins to be detached from the projectile, leaving it totally surrounded by water. Some water vapor may exist in the cavity, and cavitation usually happens. (Adapted from [6, p. 060803-2])

The splashing and piling up of water waves surrounding the submerged part of the aircraft are close to realism, as the motion of the free (water) surface is modeled and computed by the *volume-of-fluid method*. We have also used the *level-set method* and obtained similar graphical results. However, several other physical factors and phenomena have not been taken into account:

(1) The deceleration of the aircraft motion, as its speed is maintained at 70m/sec. In addition, in general, the presence of water will cause deflection of the flight path.

(2) At the speed of 70 m/sec, structural fracture and disintegration of aircraft are likely to occur.

(3) Hydrodynamic force, fluid buoyancy, and drag force have not been incorporated into the model.

**Box 1:** Commentary on the water-entering motion of aircraft as shown in Figure 2 and its video animation.

## 3 Simulation of the Ditching/Crashing of an Aircraft into Water as a Two-Phase Fluid-Structure Interaction Problem

Aircraft crashworthiness and human survivability are of utmost concerns in any emergency landing situation. The earth is covered 71% by water and many major airports are situated oceanside. Therefore, the likelihood of water entry is larger than that of crashing on land.

Assume that an aircraft such as MH370 did not have a mid-air explosion. Then all available signs indicate that it crashed somewhere in the Indian Ocean. This is an aircraft water-entry problem. Our objective in this section is to conduct numerical simulations for several hypothetical scenarios using CFD.

For a representative Boeing 777 aircraft, we use the values of parameters as given in Table 1.

| | |
|---|---|
| Total weight | $1.8 \times 10^5$ kg |
| Wing span | 60.9 m |
| Fuselage cross section | 29.6 $m^2$ |
| Length | 63.7 m |
| Roll Moment of Inertia | $1.06 \times 10^7$ kg $m^2$ |
| Pitch Moment of Inertia | $2.37 \times 10^7$ kg $m^2$ |
| Yaw Moment of Inertia | $3.34 \times 10^7$ kg $m^2$ |

**Table 1:** Parameter values for Boeing 777 used in CFD calculations.

| | |
|---|---|
| Atmospheric pressure | $1 \times 10^5$ Pa |
| Lower bound for pressure | $1 \times 10^4$ Pa |
| Kinematic viscosity of water | $1 \times 10^{-6}$ m$^2$/sec |
| Kinematic viscosity of air | $1.589 \times 10^{-5}$ m$^2$/sec |
| Water-air surface tension ($\gamma$) | 0.07 N/m |
| Gravitational acceleration ($g$) | 9.80665 m/sec$^2$ |
| $\rho_0$ in Equation (0.5) | 1000 kg/m$^3$ |
| Compressibility of water ($\psi_1$ in Equation (0.5)) | $1 \times 10^{-5}$ sec$^2$/m$^2$ |
| Compressibility of air ($\psi_2$ in Equation (0.6)) | $1 \times 10^{-5}$ sec$^2$/m$^2$ |
| Constants in $k-\epsilon$ turbulence model | $C_\mu = 0.09$, $C_1 = 1.44$, $C_2 = 1.92$, $\sigma_\epsilon = 1.3$ |
| Initial values for $k-\epsilon$ turbulence model | $k = 0.1$ m$^2$/sec$^2$, $\epsilon = 0.1$ m$^2$/sec$^3$ |
| Initial aircraft speed relative to stationary water ($V_0$) | 58 m/sec ($\approx$ 130 mph) |

**Box 2:** Parameter values for fluid flow used in CFD calculations.

From the CFD point of view, the water-entry problem is characterized as *fluid-structure interaction with a free fluid-gas interface*. Water and air are modeled as compressible flows using the Navier-Stokes equations. Our mathamatical model is similar to that in Guo et al. [12].

The CFD software we have adopted here is *OpenFOAM*, which is open-source and now widely used by industry and research communities. See an introductory article by several of us in [13]. In particular, we will be using `compressibleInterDyMFoam` for two-phase flow, and RANS $k-\epsilon$ for *turbulence modeling*. Computations were performed on the EOS supercomputer at Texas A&M University and RAAD supercomputer at Texas A&M University at Qatar. For the computational work shown in the examples of this section, each run took one to several days on the campus supercomputers.

# OpenFOAM for Computational Fluid Dynamics

Goong Chen[1], Qingang Xiong[2], Philip J. Morris[3], Eric G. Paterson[4], Alexey Sergeev[5], and Yi-Ching Wang[6]

## 1. Introduction

There is a revolution going on, impacting and transforming how computational mechanics and the associated design and optimization are done: the emergence, availability, and large-scale use of *OpenFOAM* [1]. It belongs to the contemporary *open-source trend* not unlike the roles played by the Linux operating system or the Internet encyclopedia Wikipedia. OpenFOAM is free and is used by thousands of people worldwide in both academic and industrial settings. The acronym OpenFOAM stands for *Open Source Field Operation and Manipulation.*

Computational mathematics and mechanics provide fundamental methods and tools for simulating physical processes. Numerical computation can offer important insights and data that are either difficult or expensive to measure or to perform tests experimentally. What is more, numerical computation can simulate supernova explosions and galaxy formations, which can not be produced in earth-bound laboratories. It has been recognized for at least 30 years that *computational science* constitutes a third and independent branch of science, on equal footing with *theoretical and experimental sciences*. Cutting across disciplines at the center of computational science

[1]Goong Chen is professor of mathematics at Texas A&M University (TAMU) and Texas A&M University at Qatar (TAMUQ). He is also a member of the Institute for Quantum Science and Engineering at TAMU. His email address is gchen@math.tamu.edu.

[2]Qingang Xiong is postdoctoral researcher of mechanical engineering at Iowa State University. His email address is xiong@iastate.edu.

[3]Philip J. Morris is Boeing/A.D. Welliver Professor of Aerospace Engineering at The Pennsylvania State University. His email address is pjm@psu.edu.

[4]Eric G. Paterson is Rolls-Royce Commonwealth Professor of Marine Propulsion and department head of Aerospace and Ocean Engineering at Virginia Tech. His email address is egp@vt.edu.

[5]Alexey Sergeev is postdoctoral fellow of mathematics at TAMU and TAMUQ. His email address is asergeev@asergeev.com.

[6]Yi-Ching Wang is PhD student at the Mathematics Department of TAMU. Her email address is ycwang@math.tamu.edu.

We assume that the aircraft is a *rigid body*. Except for the sample case shown in Figure 2, we did not include the under-wing engines in the Boeing 777 aircraft, with the understanding that the strut-mounted engine nacelles would likely be the first things to be torn off in a water-entry situation. (But, computationally, it is straightforward to include the engines in our CFD work, such as shown in Figure 2.)

There are two distinct CFD features of this problem:

(1) Because of the *relative motion* between the aircraft and water, *dynamic mesh*, or a non-inertial frame of reference, must be used. Here we have used a combination of `dynamicRefineFvMesh` and `dynamicMotionSolverFvMesh` in OpenFOAM for this purpose.

(2) The *free water surface* can be treated by using either the *volume of fluid method* [14] (VOF), the *level set method* [15, 16], a combination of these two methods [17] or the *cubic interpolated pseudoparticle method* [18]. Because of the availability of the software for VOF in OpenFOAM, VOF is adopted here.

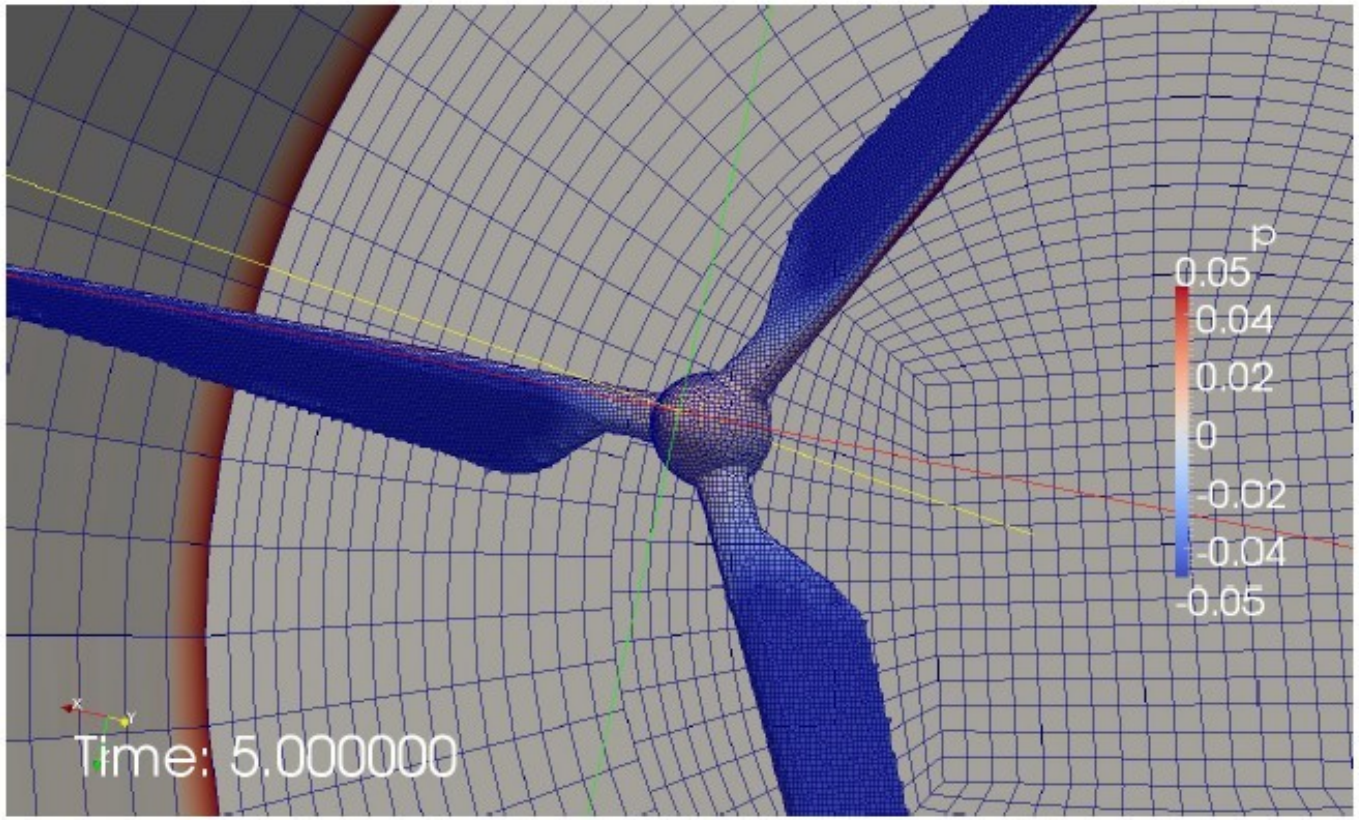


Figure: The pressure distribution on the rotor blade's surface at $t = 5$ for Example 1. Note that the rotor's radius is 2m, while the grids within the inner radius 2.5m are *rotating* with the rotor. There is a *mismatch* with fixed the exterior cylindrical grids. The exterior cylindrical domain extends to radius 5.0m.

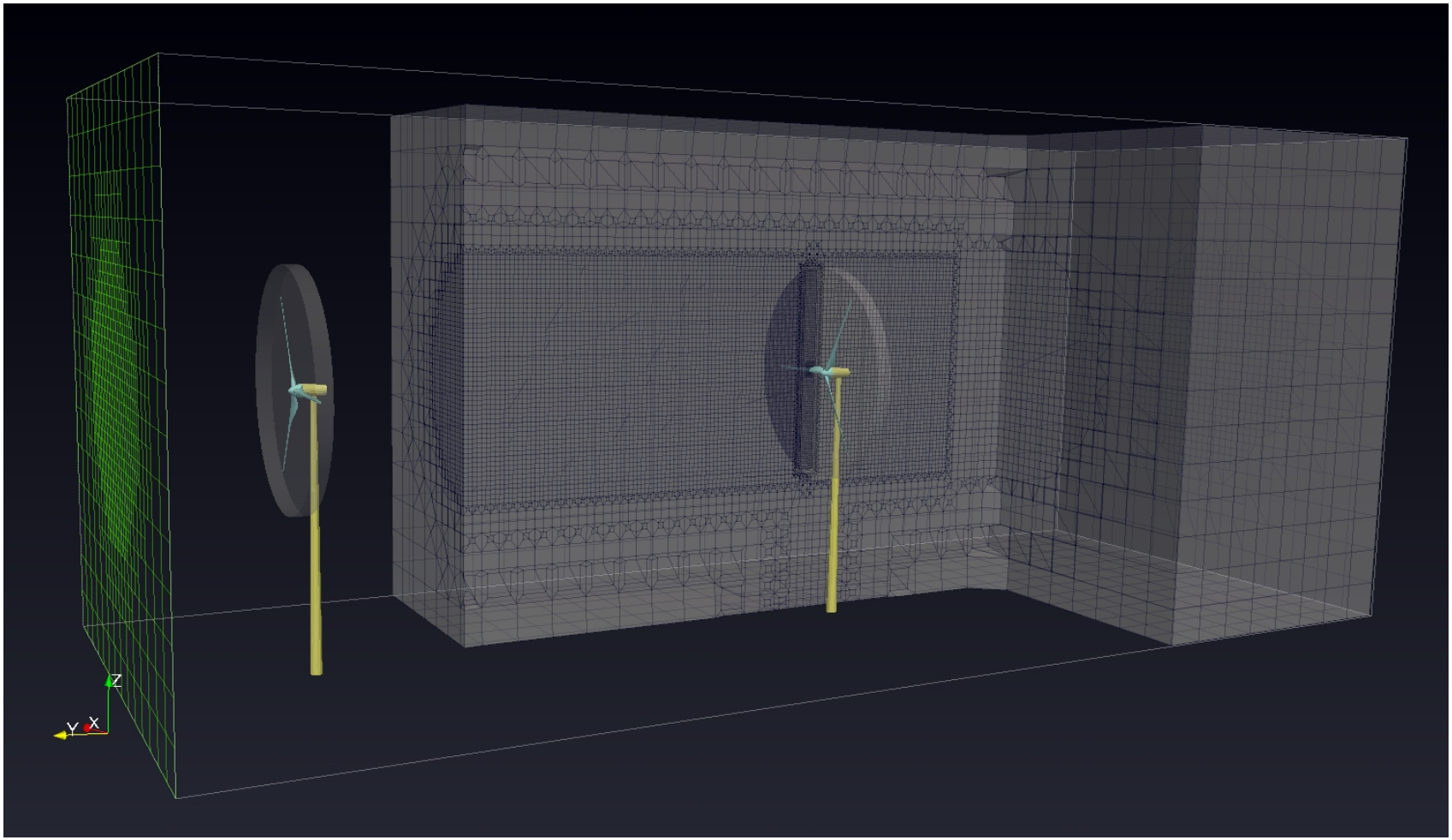
Z
Y
X

Equations for the volume of fluid two-phase problem are the following:

- (Conservation of mass for each phase)

$$\frac{\partial(\rho_i \alpha_i)}{\partial t} + \nabla \cdot (\rho_i \alpha_i \mathbf{u}) = 0, \tag{0.2}$$

where $\alpha_i$, $i = 1, 2$, are volume fractions of each phase satisfying $\alpha_1 + \alpha_2 = 1$.

- (Conservation of momentum)

$$\frac{\partial(\rho \mathbf{u})}{\partial t} + \nabla \cdot (\rho \mathbf{u}\mathbf{u}) - \nabla \cdot (\mu(\nabla \mathbf{u} + \nabla \mathbf{u}^{\mathsf{T}})) = -\nabla p + \rho \mathbf{g} + \gamma \kappa \nabla \alpha, \tag{0.3}$$

where $\rho$ and $\mu$ are effective density and viscosity fields for the mixture, $\gamma$ is the surface tension and $\kappa$ is phase interface curvature

$$\kappa = -\nabla \cdot \left( \frac{\nabla \alpha}{|\nabla \alpha|} \right). \tag{0.4}$$

- (Equation of State)

$$\rho_1 = \rho_0 + \psi_1 p \quad \text{(for water)}, \tag{0.5}$$

$$\rho_2 = \psi_2 p \quad \text{(for air)}. \tag{0.6}$$

- (Six degrees of freedom of motion)

$$\boldsymbol{\sigma} = -p\mathcal{I} + \mu(\nabla \mathbf{u} + \nabla \mathbf{u}^{\mathsf{T}}), \tag{0.7}$$

$$\mathbf{F}(t) = \text{force} = \int_{\partial\Omega(t)} \boldsymbol{\sigma}\mathbf{n}\, dS, \qquad \boldsymbol{\tau}(t) = \text{torque} = \int_{\partial\Omega(t)} \mathbf{r}\times\boldsymbol{\sigma}\mathbf{n}\, dS. \tag{0.8}$$

where $\mathcal{I}$ is the identity tensor. The exterior of the domain occupied by the aircraft is denoted as $\Omega(t)$ (depending on $t$ due to aircraft motion), and $\partial\Omega(t)$ is its boundary.

Note that at time $t = 0$, the velocity of the center of mass of the aircraft is $V_0$ along various angles of approach; cf. Table 2. This, together with equations (0.2)-(0.8), constitute the complete initial-boundary value problem for the numerical computation. Various physical and computational parameter values are listed in Table 2.

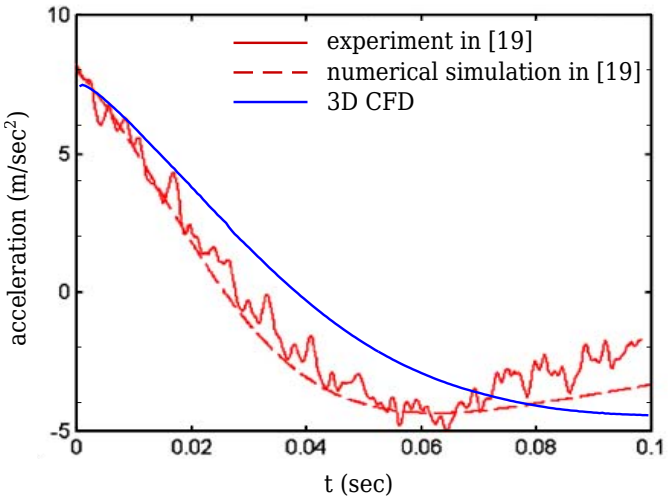


**(a)** deadrise angle is $\pi/4$, effective gravity is 8.0062 m/sec$^2$, mass of wedge is 13.522 kg, speed at water entry is 0.95623 m/sec.

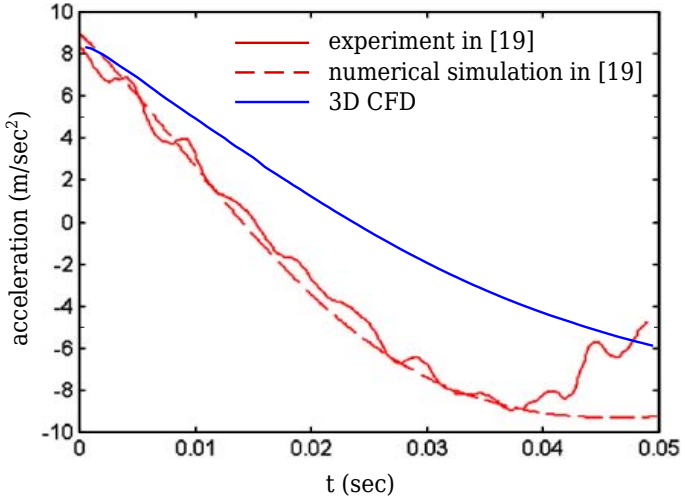


**(b)** deadrise angle is $\pi/4$, effective gravity is 8.9716 m/sec$^2$, mass of wedge is 30.188 kg, speed at water entry is 1.69673 m/sec.

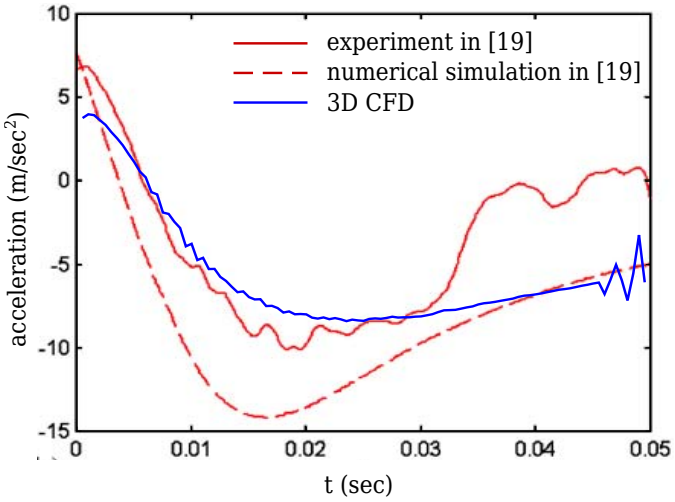


**(c)** deadrise angle is $\pi/9$, effective gravity is 7.8144 m/sec$^2$, mass of wedge is 12.952 kg, speed at water entry is 0.86165 m/sec.

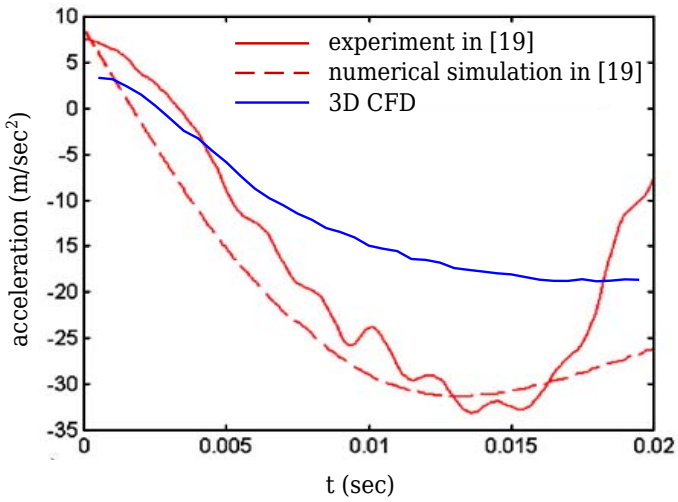


**(d)** deadrise angle is $\pi/9$, effective gravity is 8.6103 m/sec$^2$, mass of wedge is 29.618 kg, speed at water entry is 1.54405 m/sec.

**Figure 6:** Curves of acceleration versus time as benchmarks in comparisons with Wu et al. [19, p. 28]. The curves obtained from experiment and numerical simulations are compared under different settings. The blue curves represent the data obtained by our computational methods in this paper.

## Remark 0.1

Every CFD treatment needs to be validated. Here we use the experimental data available in [19] for a simplified scenario, that is, a constrained free-falling "wedge" entering water. The wedge has only the vertical translational degree of freedom. The *acceleration(/deceleration)* of the wedge is measured throughout its impact with the water. The study in [19] also employed a 2D potential flow model to study the problem numerically. In order to validate our CFD method, the setup for the experiment is replicated as a 3D mesh. Figure 6 shows the comparison of the acceleration time curves with a variety of parameters. Although some differences of values are observed, our CFD simulation shows a strong qualitative match of the acceleration/deceleration curves. We also note that the numerical model in [19] is a very simplified one without the incorporation of several aero-hydrodynamic effects.

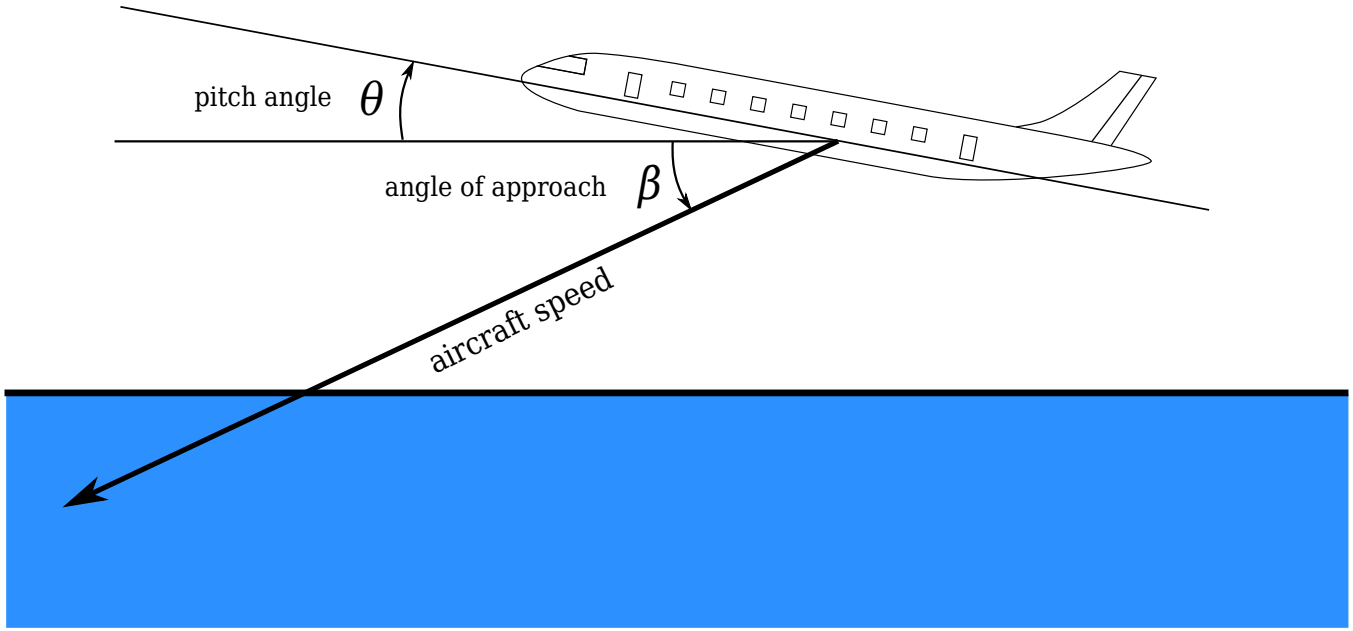


**Figure 7:** Angle $\theta$ here is the pitch angle signified in the computations of case 1-5 and $\beta$ is the angle of approach. The speed of the aircraft denotes the speed of its center of mass.

In the following, we provide snapshots and animations for visualization for different water-entry angle scenarios. Each animation consists of two parts, with the first part showing visual effects and with the second part showing pressure loading.

**Case 1:** pitch angle $= 8°$, angle of approach $= 1°$
This is what one might call *glided ditching* simil ar to the US Airways Flight 1549 mentioned in Section 1; see Figure 8 and the accompanying animation. The tail section can be seen to be subject to high pressure loading, and the water cavity in the contact area is also seen to have a *suction effect*, causing the pitch angle to *increase*. See Figure 9. This may partially explain the cause of breakoff of the tail section for the US Airways flight.

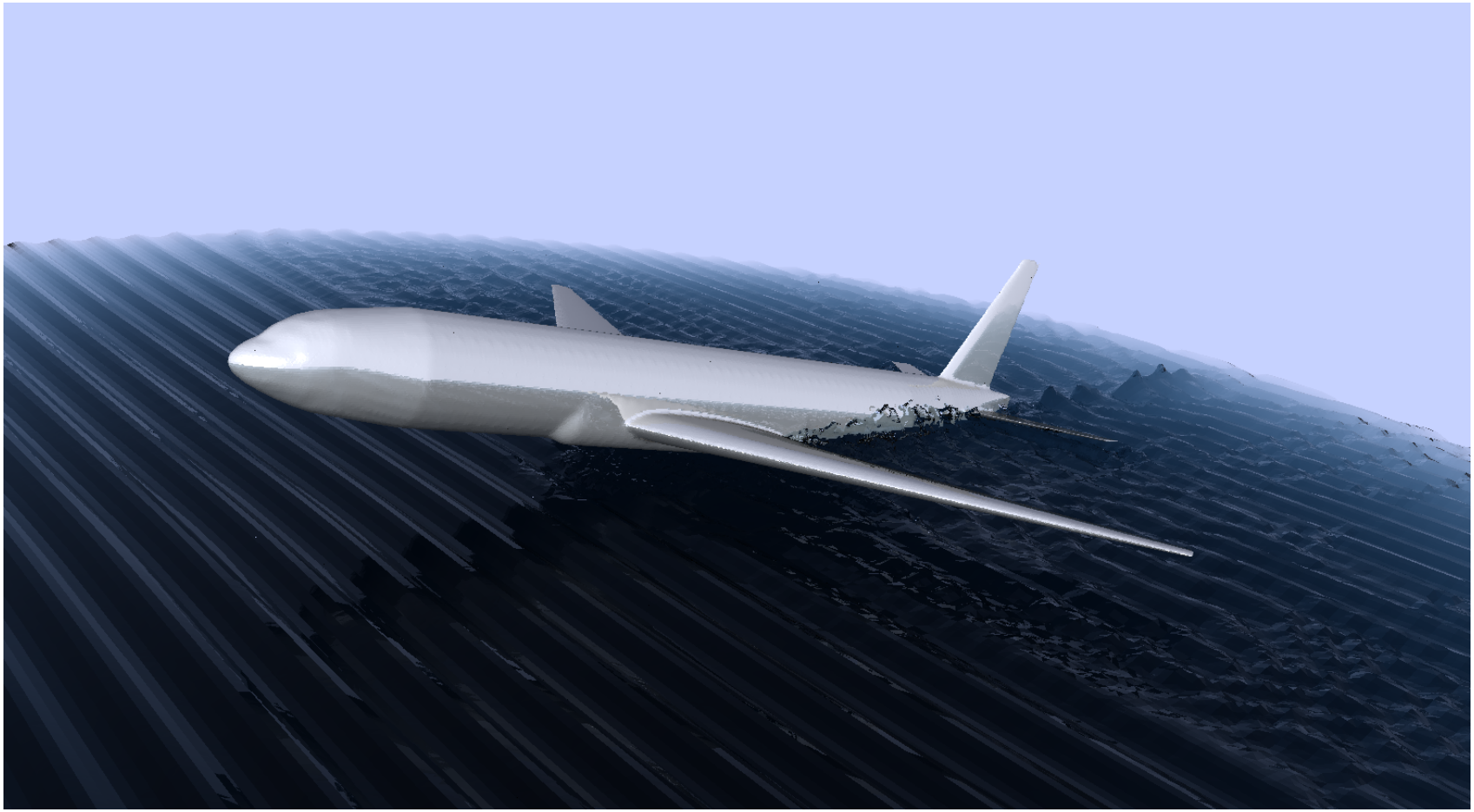

**(a)** gliding water entry

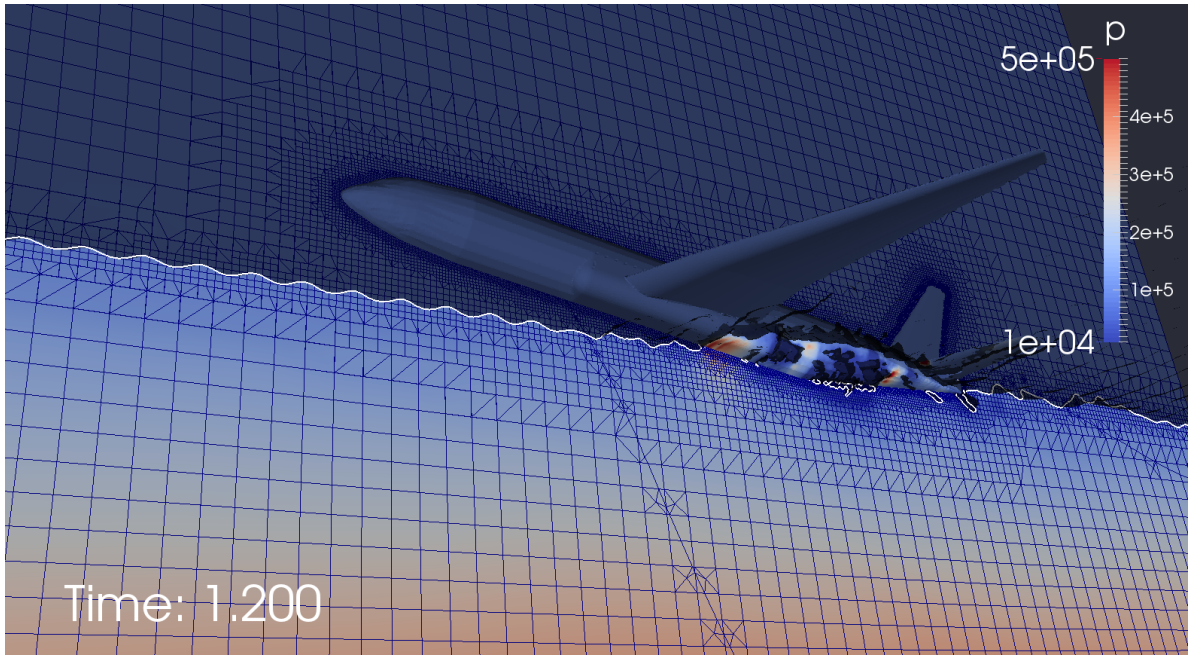


**(b)** pressure distribution and mesh

**Figure 8:** Pitch angle $= 8°$, angle of approach $= 1°$. This corresponds to **Case 1**; A video animation can be viewed at `https://www.dropbox.com/s/zpme04bmakien2h/comb8.mp4`. The animation has two parts: the first part shows the water flow pattern, while the second is intended to show the pressure distribution. (This is the same for all video animations corresponding to the remaining figures in Section 3.)

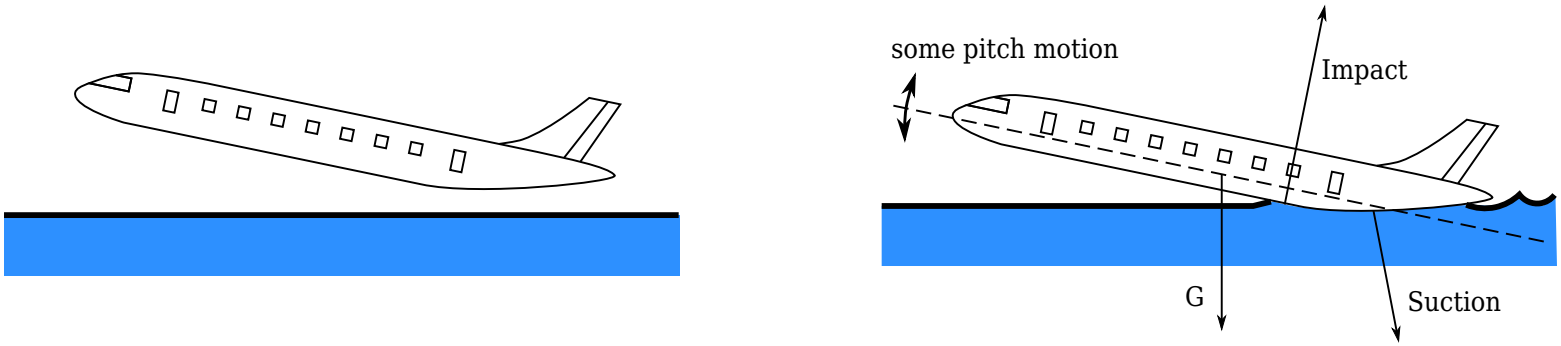


**Figure 9:** Schematics for the process of glided ditching. Major forces are illustrated. This corresponds to **Case 1**.

**Case 2:** pitch angle $= -3°$, angle of approach $= 3°$
See Figure 10 and its animation. Here we see an interesting phenomenon, namely, even though the original pitch angle is *negative*, the aircraft will "bounce" on the water and make the pitch angle *positive*. See Figure 11. At the moment this happens, the bottom of the midsection of the aircraft undergoes high surface pressure. This may cause the aircraft to break up in the middle section.

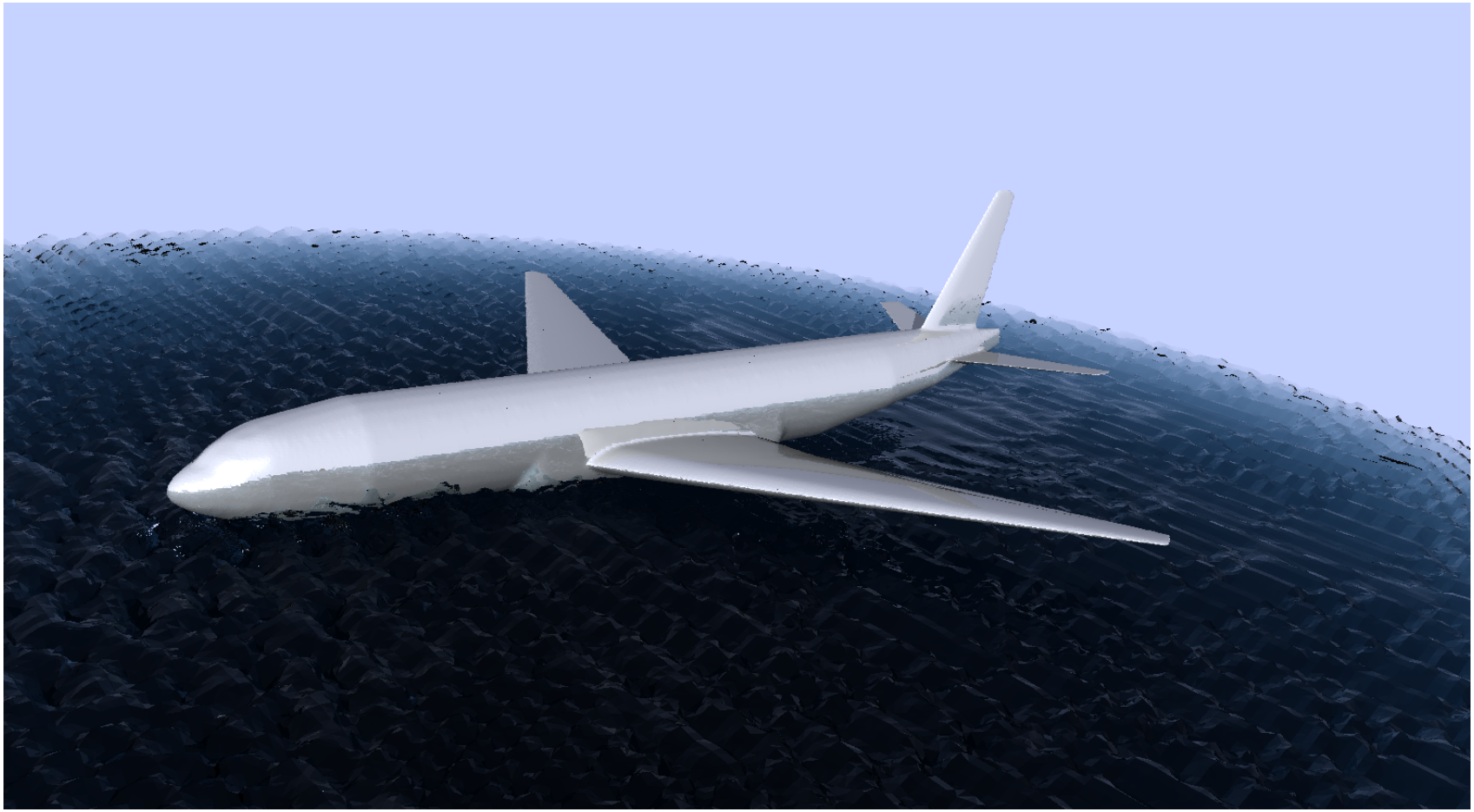

**(a)** gliding water entry (with a negative initial pitch)

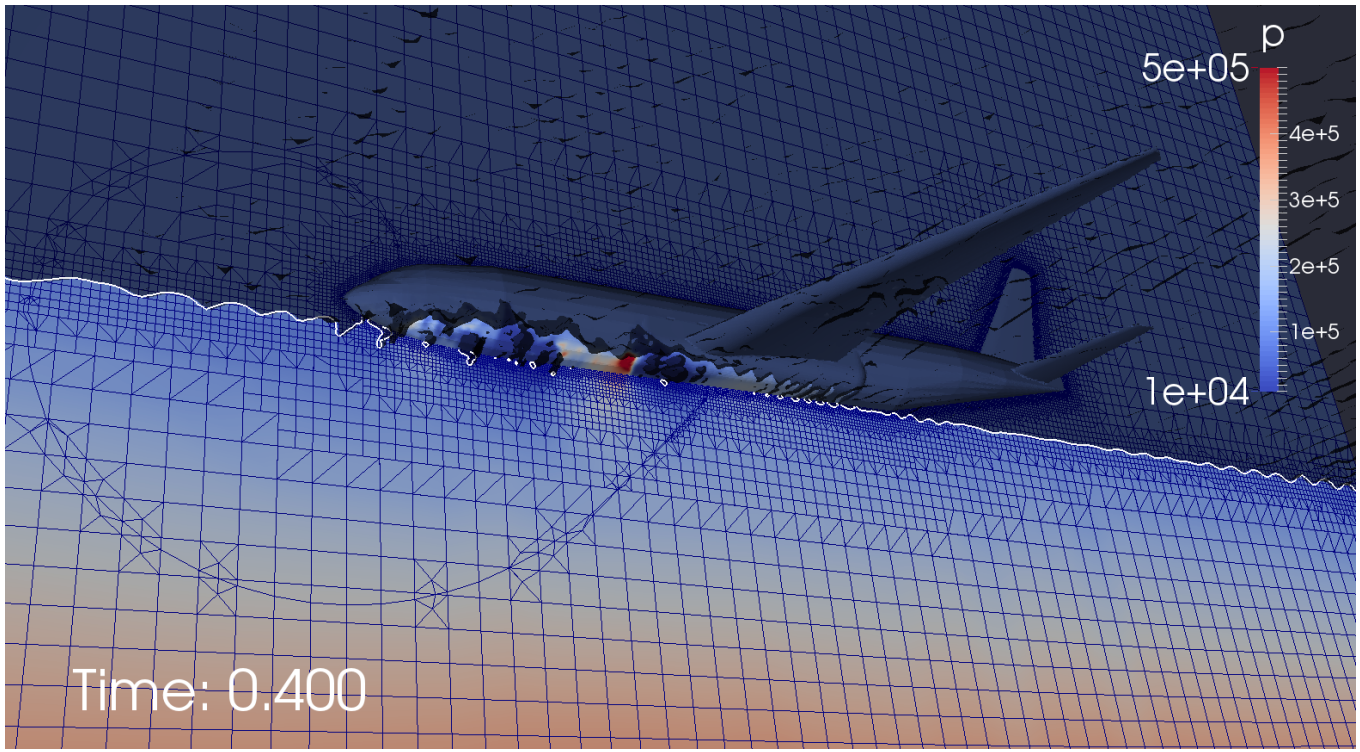


**(b)** pressure distribution and mesh

**Figure 10:** Pitch angle $= -3°$, angle of approach $= 3°$. This corresponds to **Case 2**. A video animation can be viewed at
`https://www.dropbox.com/s/6zakw7js7kbcwed/comb-3.mp4`.

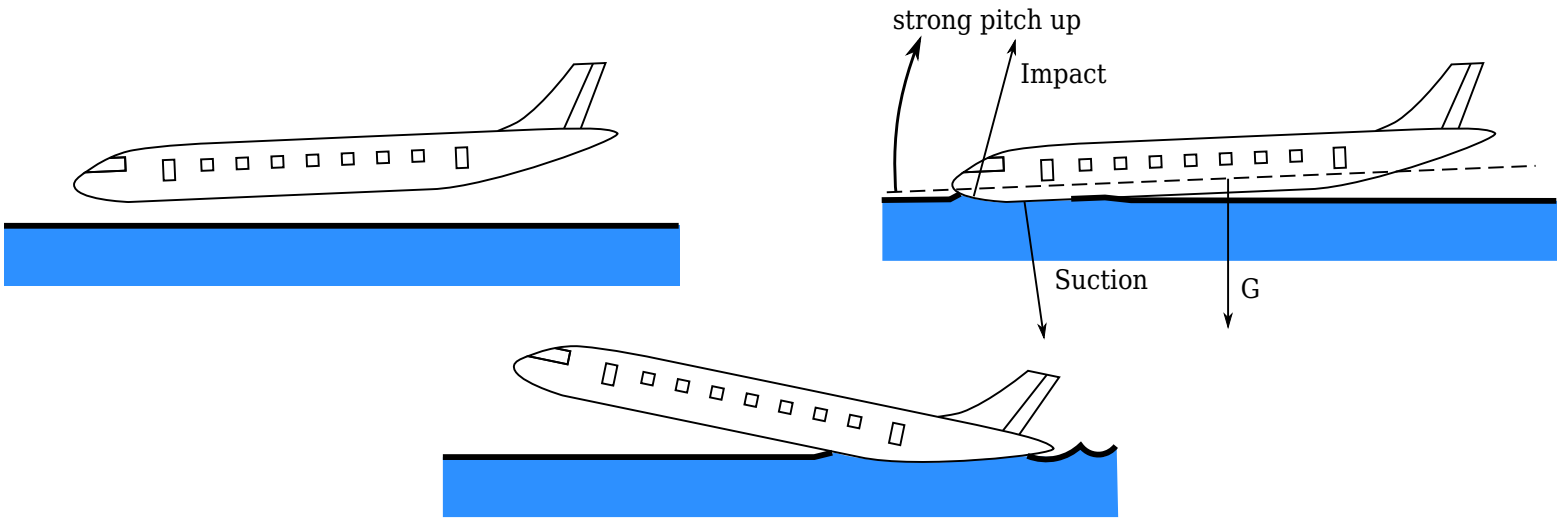


**Figure 11:** Schematics for the process of ditching with negative initial pitch. The plane is able to recover to the glided ditching attitude similar to Figure 9. This corresponds to **Case 2**.

**Case 3:** pitch angle $= -30°$, angle of approach $= 30°$
See Figure 12 and its animation. Here we see that the aircraft nose is subject to high pressure throughout the time sequence. See also the schematics in Figure 13 in contrast to Figure 11. Also, once the wings enter the water, the leading edge of the wing also is subject to high pressure loading.

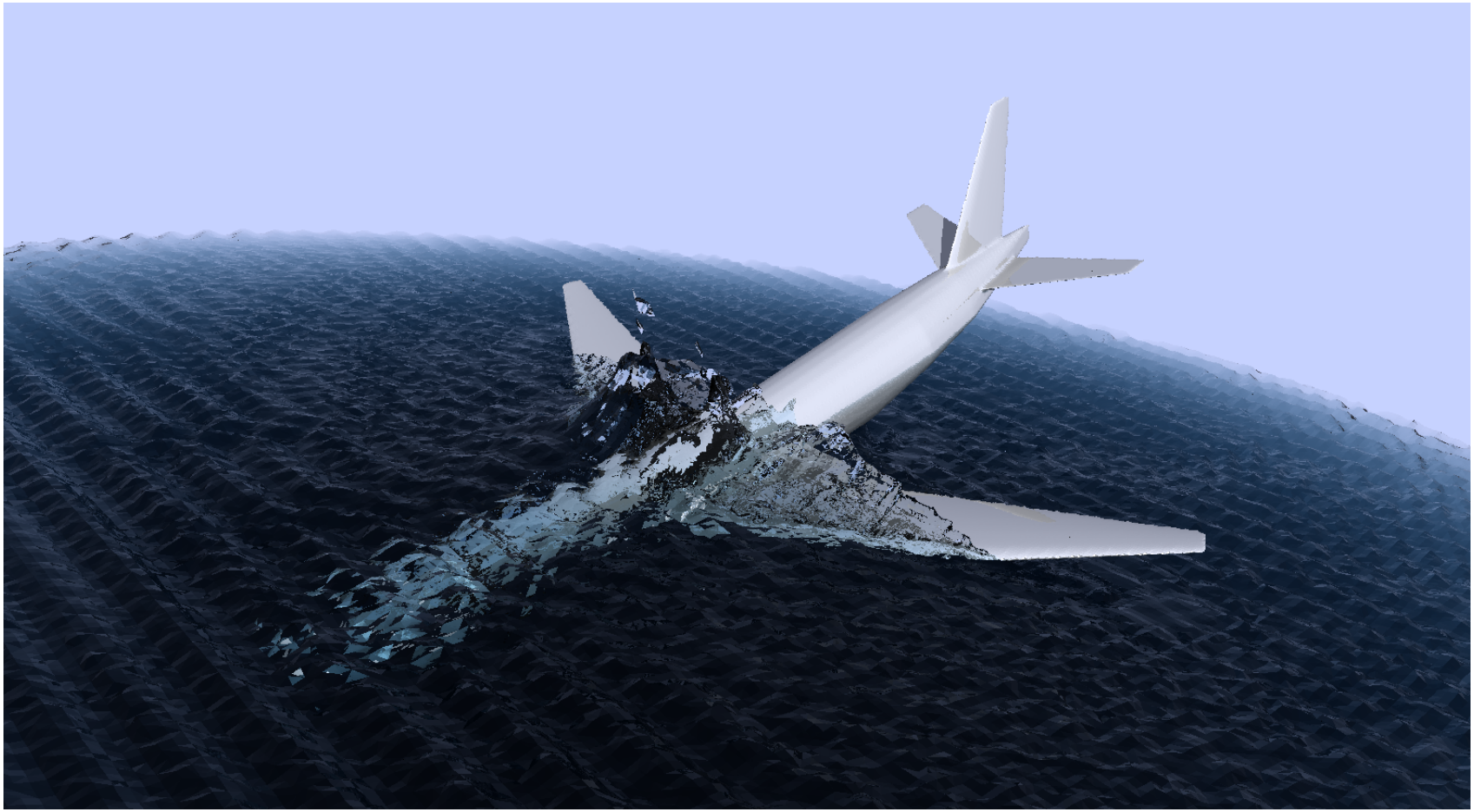

**(a)** diving water entry

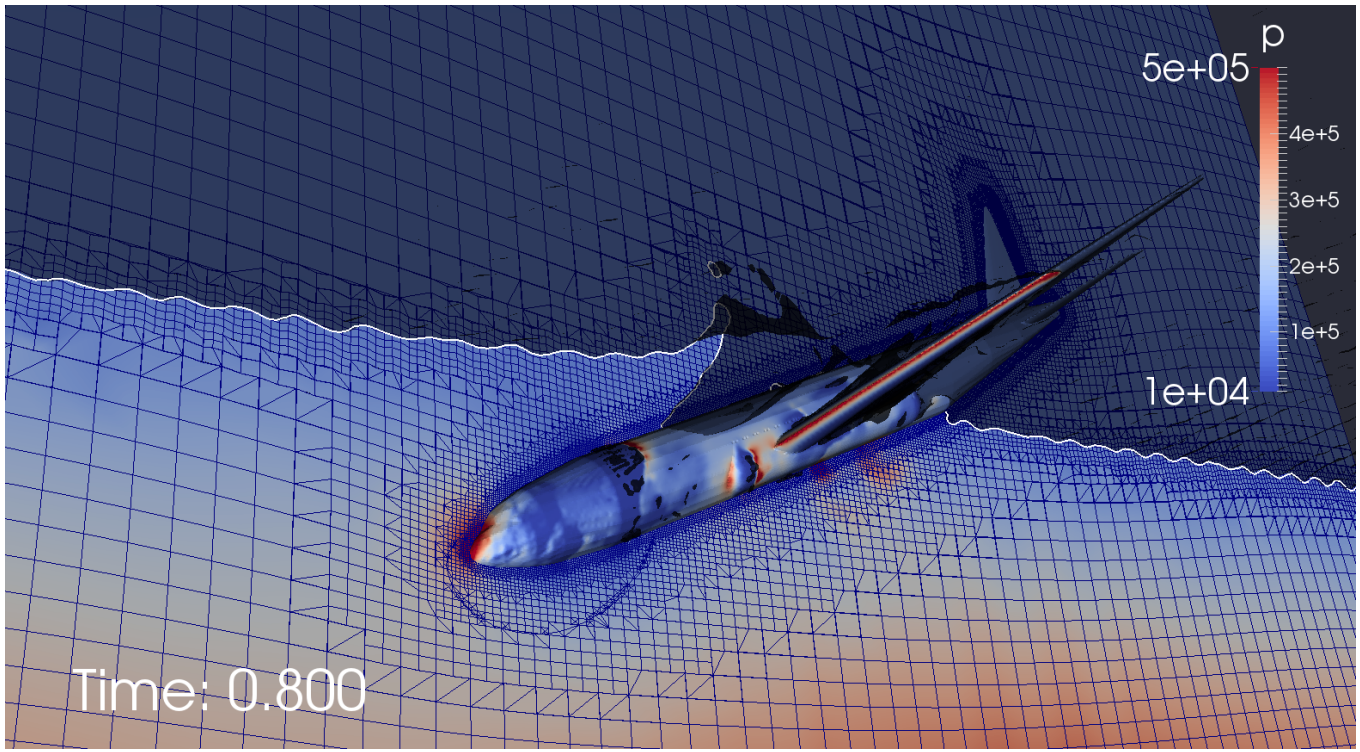


**(b)** pressure distribution and mesh

**Figure 12:** Pitch angle $= -30°$, angle of approach $= 30°$. This corresponds to **Case 3**. A video animation can be viewed at `https://www.dropbox.com/s/8iyj9xws4d90avk/comb-30.mp4`.

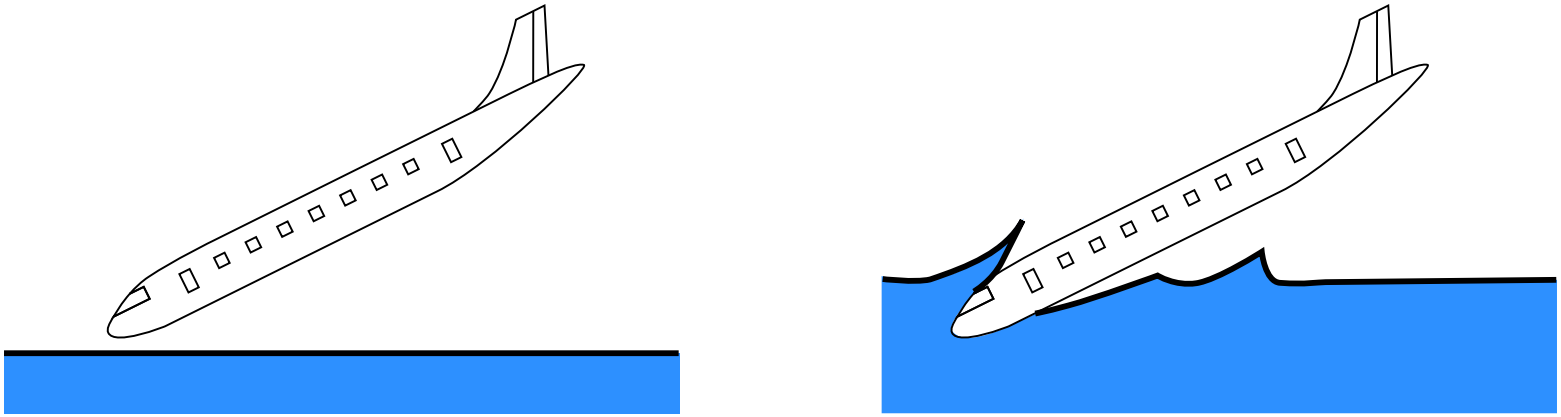

**Figure 13:** The pitch angle is too negative to recover to the glided ditching attitude. The plane's nose dives into the water with little bouncing motion. This corresponds to **Case 3**.

**Case 4:** pitch angle $= -90°$, angle of approach $= 93°$
See Figure 14 and its animation. This is a *nose-dive* situation. (For example, if an aircraft stalls when in a climb or if a control surface - ailerons, rudder and stabilizers - malfunctions, the aircraft may nose-dive.) Here we further assume that the ocean current flows from left to right at a velocity of 3 m/sec. Then once the aircraft enters the water, the current gradually drives the aircraft toward the 5 o'clock direction. Eventually this could cause it to fall on the ocean floor *belly-up*. See Figure 15.

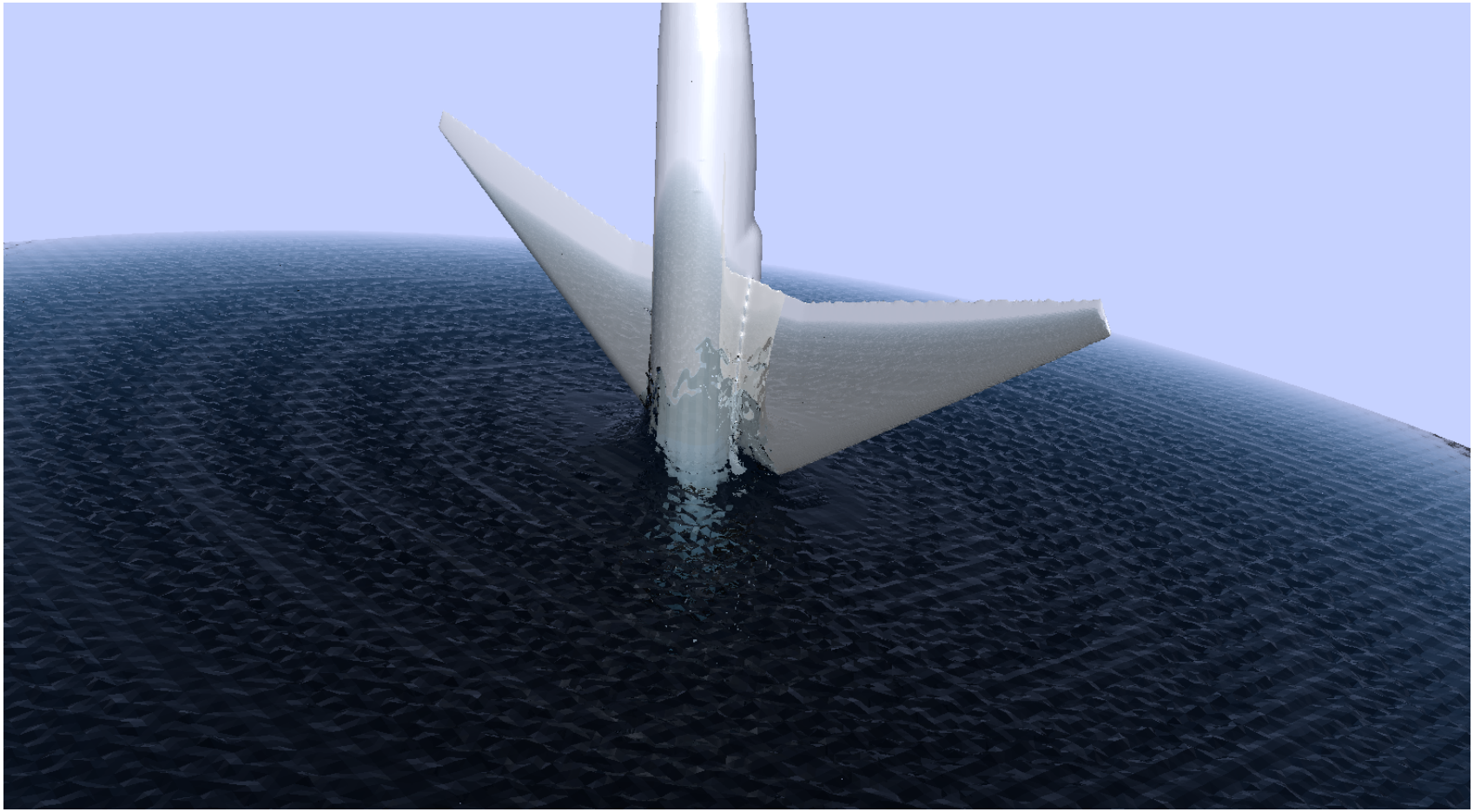

**(a)** nose-dive water entry

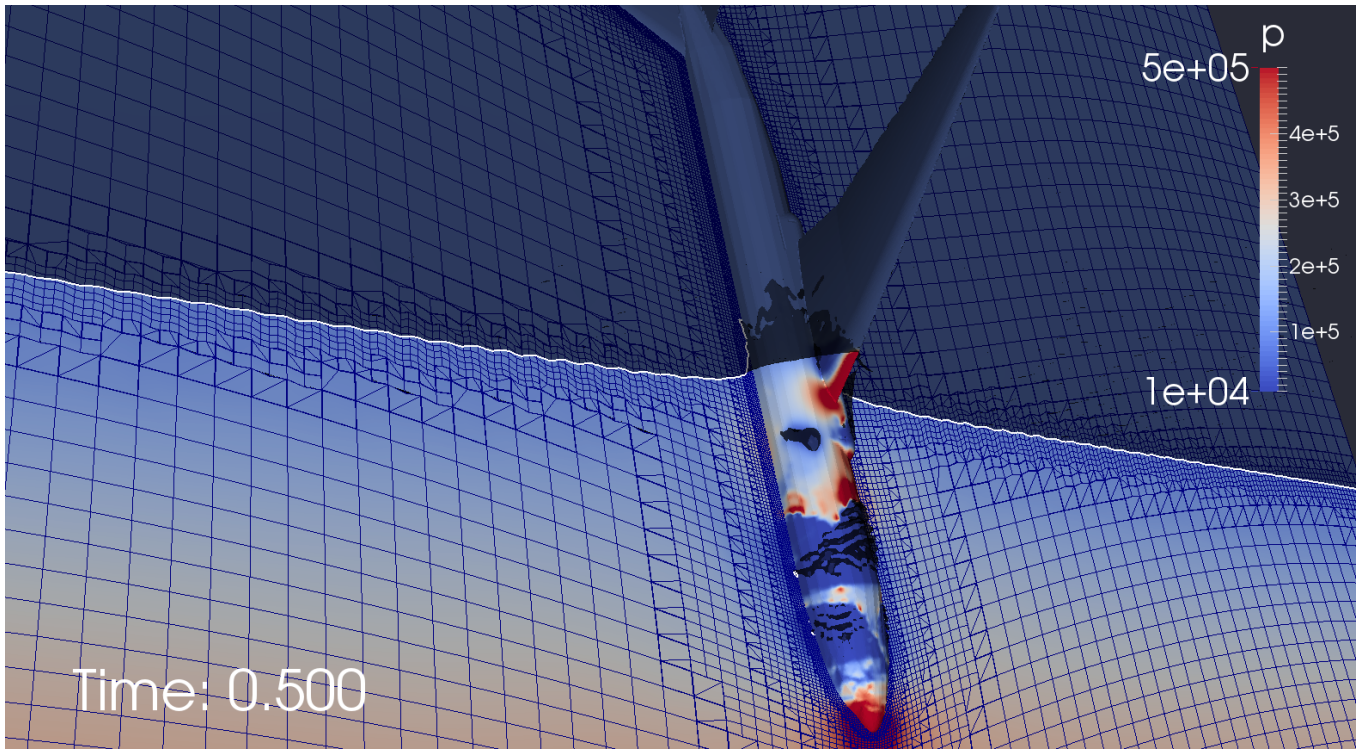


**(b)** pressure distribution and mesh

**Figure 14:** Pitch angle $= -90°$, angle of approach $= 93°$. This corresponds to **Case 4**. A video ideo animation can be viewed at `https://www.dropbox.com/s/vaf0qenjw0lk5yz/comb-90.mp4`.

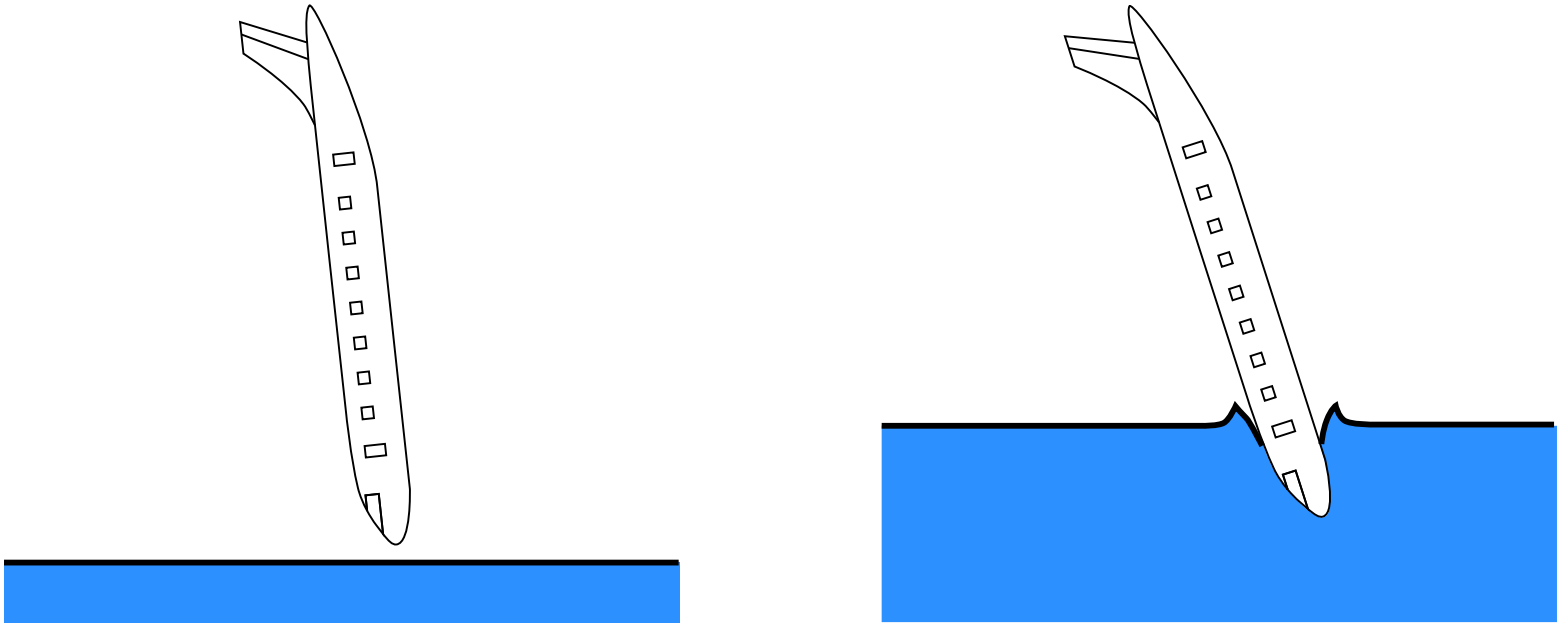

**Figure 15:** Schematics for nose-diving. The ocean current pushes the aircraft to the right, causing it possibly to finish belly up on the ocean floor. This corresponds to **Case 4**.

**Case 5:** pitch angle $= -3^\circ$ with roll angle $= 20^\circ$,
angle of approach $= 3^\circ$
See Figure 16 and its animation. Here, with a 20 degree roll, the left wing of the plane enters the water first. Almost inevitably, this would cause structural failure of the left wing.

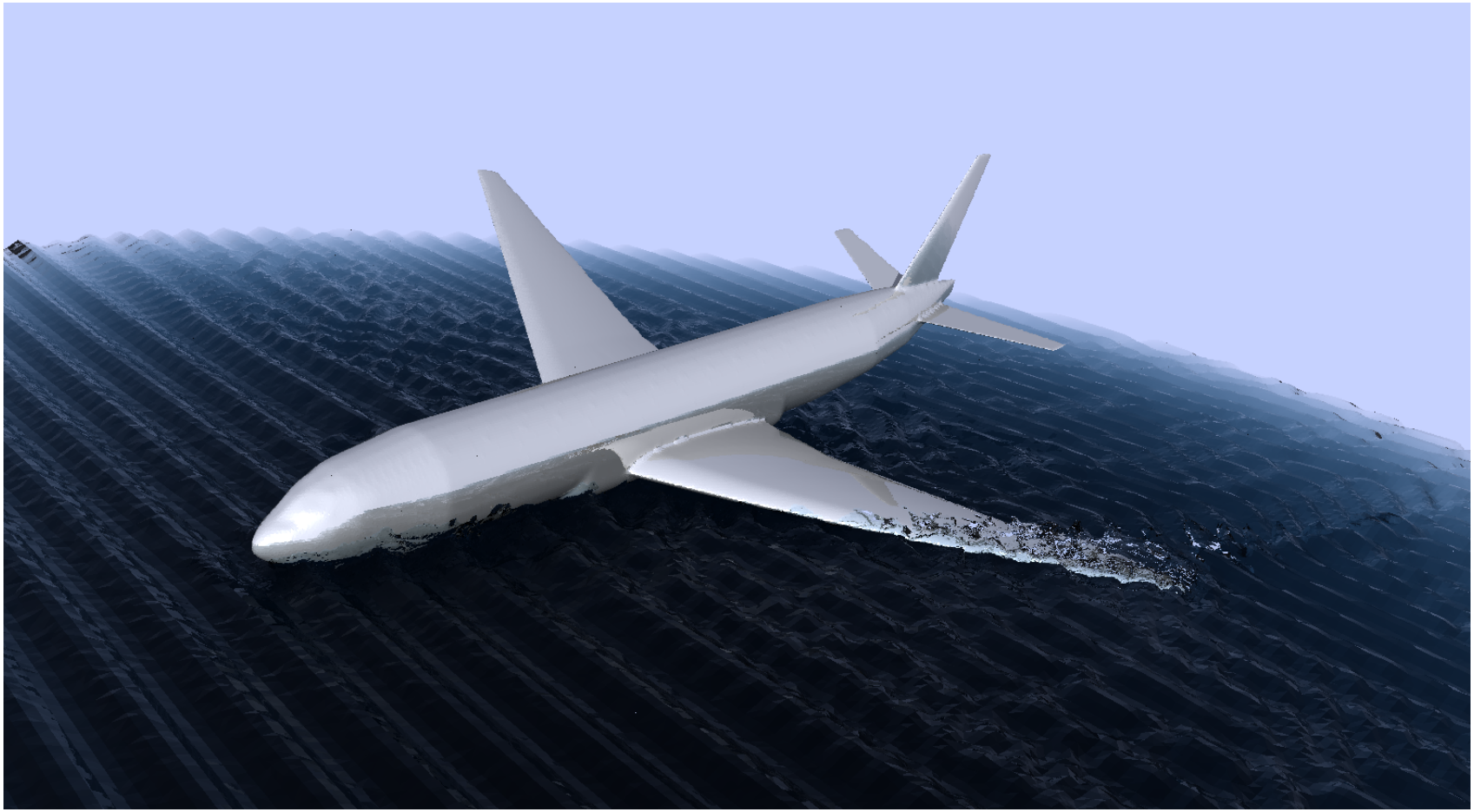

**(a)** rolling water entry

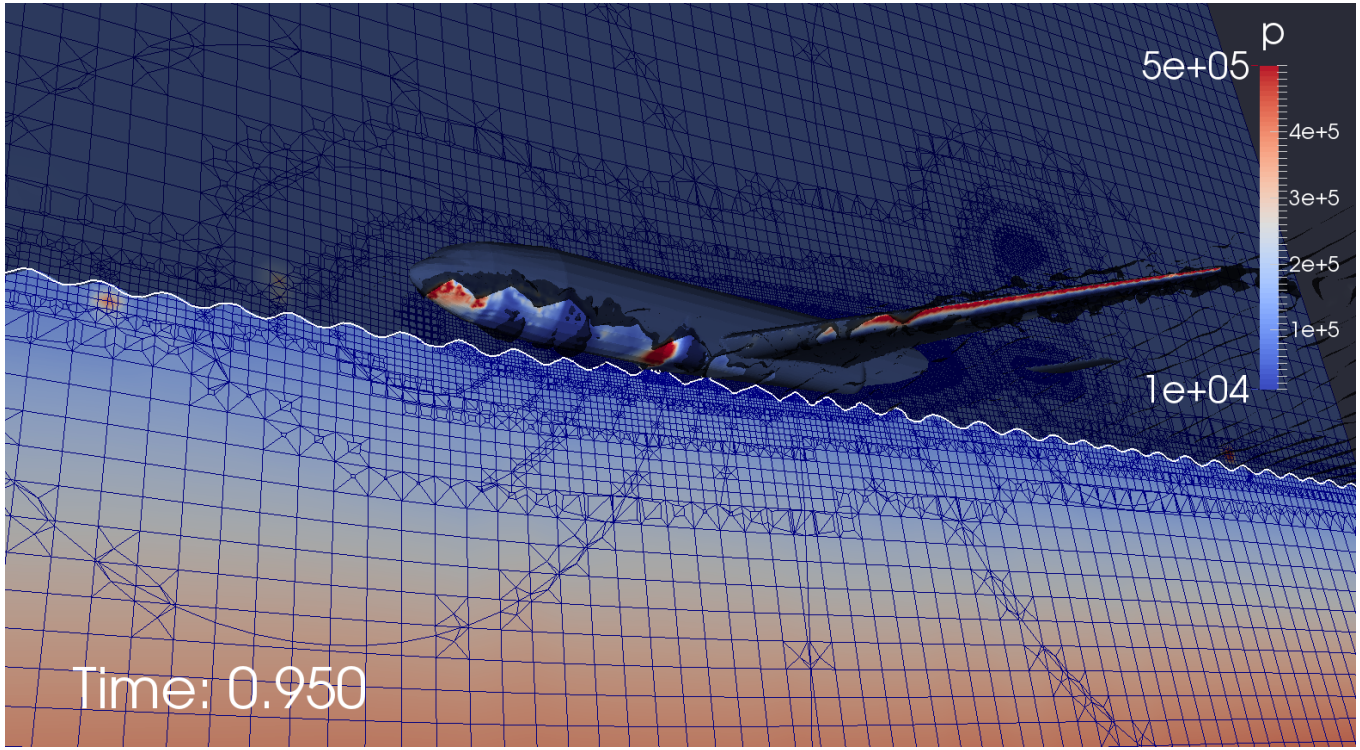


**(b)** pressure distribution and mesh

**Figure 16:** Pitch angle $= -3°$, angle of approach $= 3°$, but with a left-roll angle of $20°$. This corresponds to **Case 5**. A video animation can be viewed at `https://www.dropbox.com/s/cgvn99okc4ao0i4/combSide.mp4`.


**Figure 17:** Ethiopian Airliner crash after hijack, with rolling entry into water near Comoros Island.

`http://www.youtube.com/watch?v=sKC9C0HCNH8`

## 4 Breakup or No Breakup

As described in the Introduction, not all emergency water landings end in disaster. The dramatic successful landing in the “Miracle on the Hudson” is such a case. The fact that no lives were lost is a testament to the experience and fast thinking under pressure of the captain and crew. In that case the tail section did break off. The speed of the aircraft at ditching was estimated to be 150 mph (240 km/hr or 67 m/sec).

The outcome of another ditching effort was not so fortunate. On August 6, 2005, a Tuninter Airlines Flight 1153 ATR-72 aircraft, flying from Bari International Airprt, Bari, Italy, to Djerba-Zarzis Airport, in Djerba, Tunisia, ran out of fuel and ditched into the Mediterranian 43 km northeast of Palermo, Italy. Upon impact, the aircraft broke up into three pieces. Sixteen persons out of the thirty nine passengers and crew died. Eight of the deaths were actually attributed to drowning after the bodily injuries from impact.

In the numerical simulations provided in the preceding section, we have not included the effects of *rupture and structural disintegration*. But they are almost certain to happen upon the entry of the aircraft into water. This happened even in the miracle on the Hudson case with smooth gliding. The study of impact damage and breakup belongs to a field called *impact engineering*, which is based on the *plasticity* properties of solids that are totally different from fluid dynamics we have been talking about to this point.

Due to the limited scope of this article, we can't delve too much into the study of impact effects. Nevertheless, we can use another famous example, the disaster of the Space Shuttle Challenger, to understand what may happen, based on the analysis of one of the coauthors (Wierzbicki) in [20, 21].

The airframe of the Space Shuttle Challenger, an assemblage of ring and stringer-stiffened panels, was constructed essentially like a wide-body Boeing 747 airliner. This in turn is similar to a wide-body aircraft such as the example Boeing 777 under discussion here. Thus, we expect that much of the material and structural failure analysis performed in [20, 21] for Challenger continues to hold. According to [20, p. 651], there are three primary failure modes as depicted in Figure 18. Note that the *bending fracture* of rings (cf. Figure 18(a)) can happen even at *low impact velocities*, as has been demonstrated with a real model of a retired aircraft in DYCAST (Dynamic Crash Analysis of Structures) by NASA [22]. These findings were published nearly three decades ago but still remain valid today.

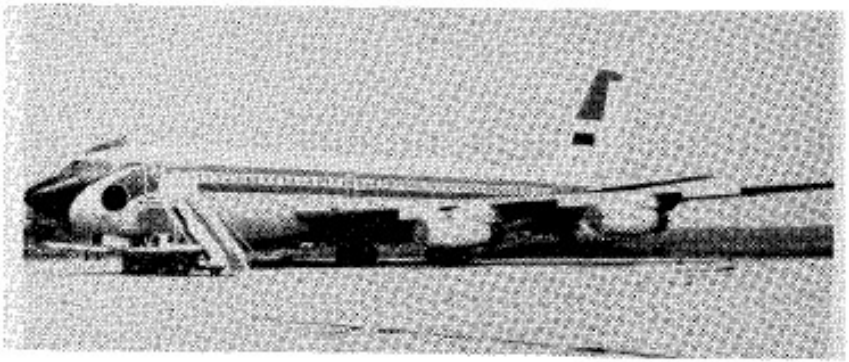

Fig. 1 Boeing 720 transport used in CID.

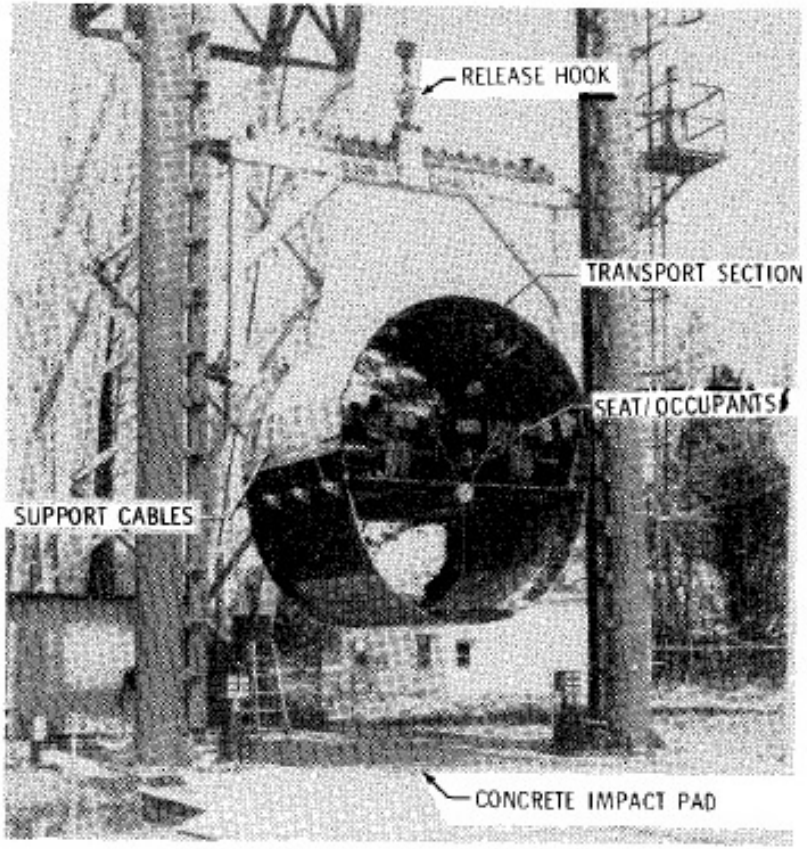


Fig. 2 Forward transport section in drop tower.

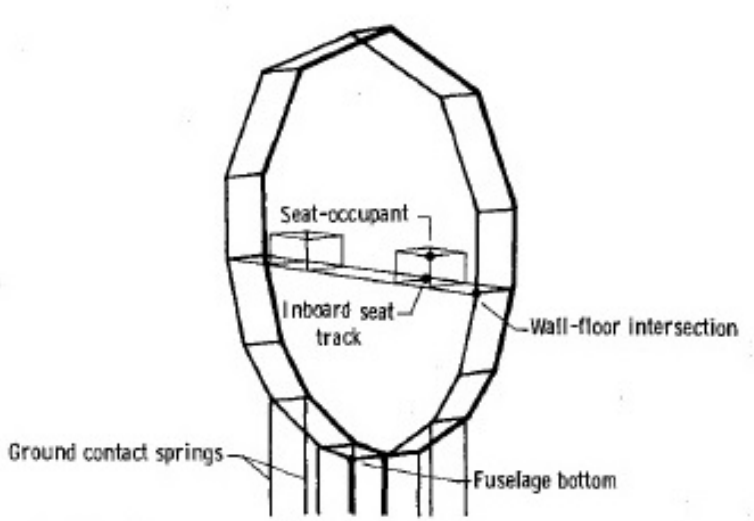


Fig. 3 Two-frame model showing nodes where responses are compared.

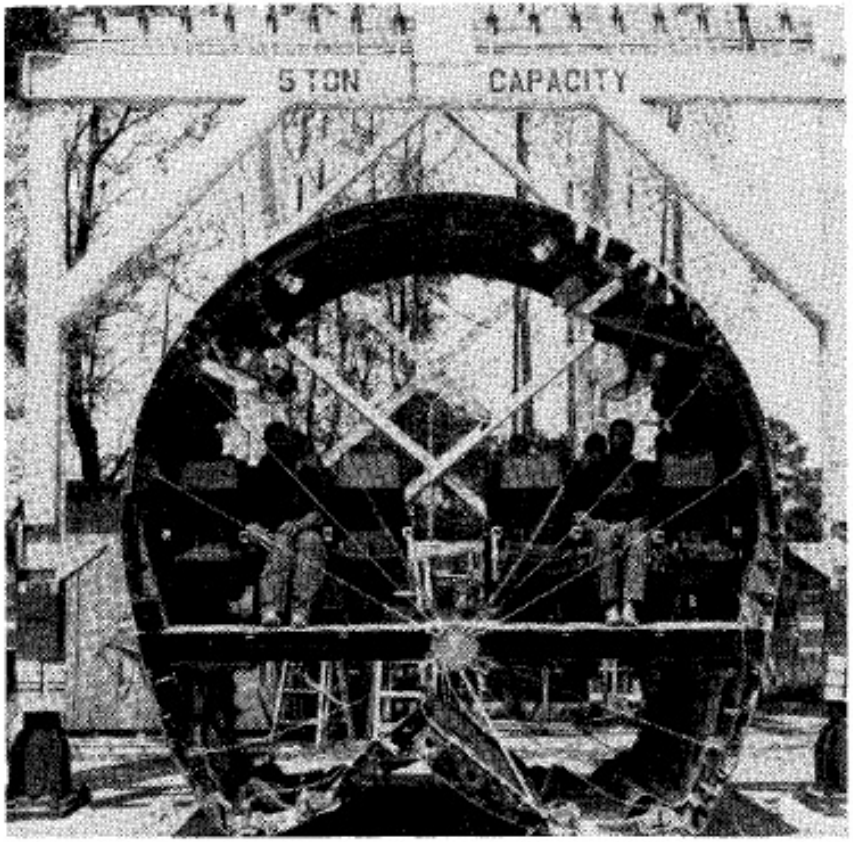


Fig. 4 Forward transport section showing post-test damage.

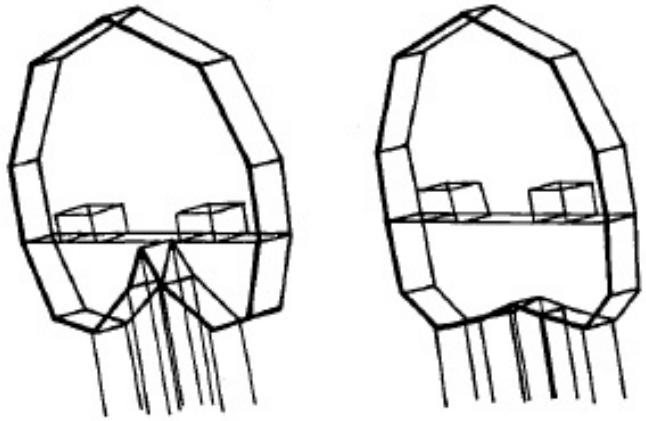

(a) Failure strain .05 (b) Failure strain .08

Fig. 5 Effects of beam failure strain at time 0.23 s after impact.

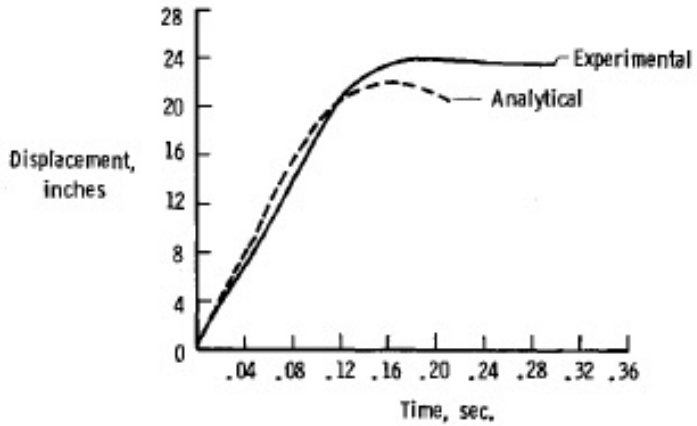


Fig. 6 Comparison of vertical floor displacements.

*Fracture failure* mode (Figure 18(b)) is estimated to happen when the vertical component of velocity exceeds 18.8 m/sec upon water entry [20, p. 652]. Rupture of fuselage and wings as shear and tensile cracks will be initiated and then propagate through the stiffened shell, leading to global structural failure. This is a dynamic process whose analysis is very challenging. Nevertheless, the *shear failure* mode, Figure 18(c), happens at a much larger impact velocity (than 18.8 m/sec) and, thus, is probably not a primary failure factor.

In addition to structural rupture and disintegration, the *acceleration due to free fall* and the *deceleration due to the impact of the structure* are important for human survival in a crash. In [20], it was analyzed that if the vertical component of the terminal impact velocity lies in the range of 62.5 m/sec and 80.5 m/sec, maximum decelerations could reach in the order of 100g to 150g (g is the gravitational acceleration constant) over a short period of time, within a regime labeled “severe injuries” [20, 23] by NASA.

As a consequence of this, it now becomes clear that *the vertical component of the terminal water-entry velocity should be reduced as much as possible*, such as the glided water-landing approach taken by Captain Sullenberger for US Airways Flight 1549 on the Hudson River. That is, some "pitching attitudes" of the aircraft will have a much higher probability of survival by averting structural damage and decelerations of the occupants [21, p. 34]. Indeed, according to Guo, et al. [12], it is recommended that for a transport aircraft with a low horizontal tail, the pitch angle be chosen between 10° and 12° for safer ditching. Such knowledge enhances air travel safety, and, as shown here, can be obtained by CFD simulations.

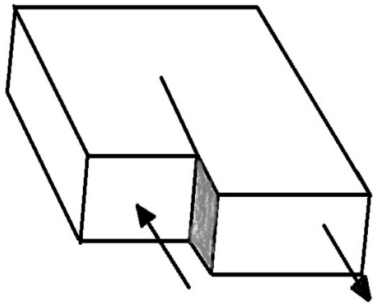

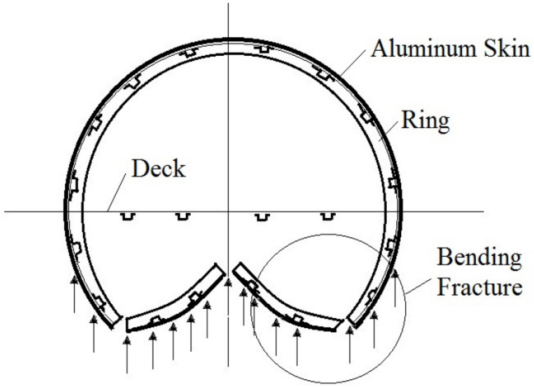
Aluminum Skin
Ring
Deck
Bending
Fracture

**(a)**

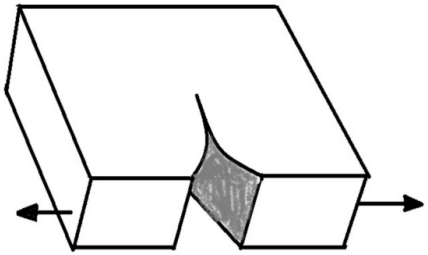

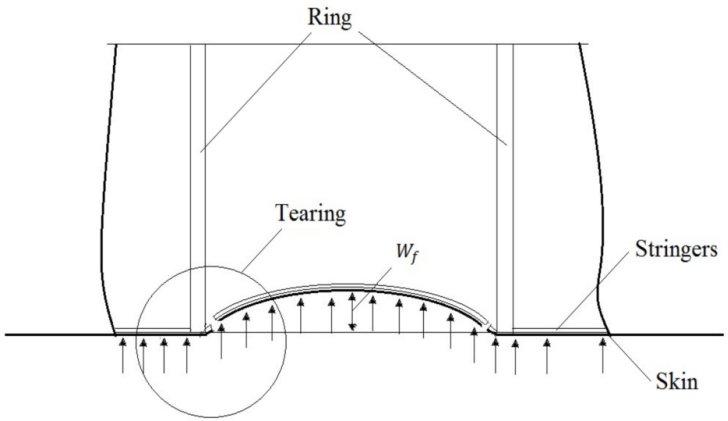
Ring
Tearing
$W_f$
Stringers
Skin

**(b)**

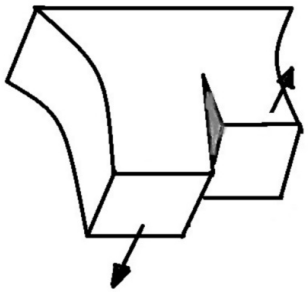

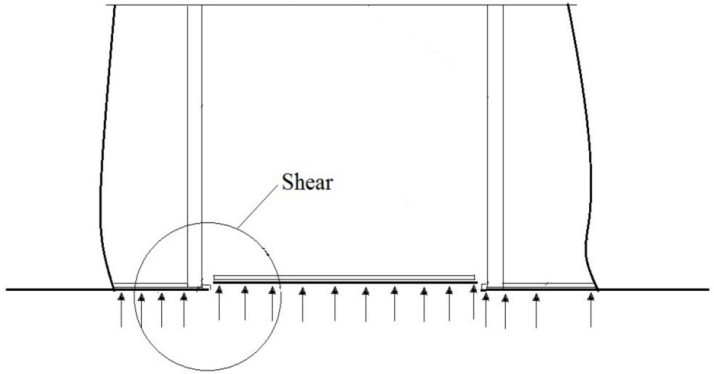


**(c)**

**Figure 18:** Three modes of structural failure for a wide-body airliner: (a) flexural failure of rings; (b) tearing fracture; and (c) shear of the longitudinally stiffened shell. (Adapted from [20, p. 651])

## 5 Concluding Remarks

The crash of an airliner into ocean is a profoundly tragic event. But on the mathematical and engineering side, there should be significant interest in its modeling and computation so that one can understand the physical mechanisms better in the hope of improving aircraft crashworthiness and survivability. The CFD approach is advantageous in saving long and expensive processes of laboratory setup and measurements. Now, with the availability of more abundant free and open-source computational tools and user-friendly software, it has become much easier for mathematicians to conduct interdisciplinary collaboration with engineers and physicists, just as this article has hoped to demonstrate. Many chanllenges remain. Regarding CFD for the study of aircraft ditching in water, see an excellent review and outlook paper in Liu et al. [24].

A large body of literature already exists for the computer simulation of *rupture and disintegration* of a crashing aircraft. But this work requires considerably more effort and time, which is presently beyond the resources of the authors. For example, the software by Abaqus [25], LS-DYNA [26] and others is known to be able to simulate the impact and breakup of solids in collisions. But this component of the problem is beyond the scope of the present article. Interested readers are certainly welcome to delve into this topic and gain further insights and understanding on the subject.

On any given day, there are now hundreds of thousands of people traveling by air worldwide. Air travel has never been safer and continues to become even safer. According to Barnett [27] in the 2000-2007 time period the death risk per flight on a First-World airliner was 1 in every 2 million: and 2 million days is nearly 5,500 years! There are always bound to be unfortunate and tragic incidents. However, it is to be expected that data generated by numerical simulations will further improve passenger survival in emergency water landings.

## Acknowledgement

We thank the generous supports from the Qatar National Research Funds grant National Priority Research Project #5-674-1-114 and Texas A&M University's internal grant for interdisciplinary research CRI Scully funds through the Institute for Quantum Science and Engineering. We also thank the staff at TAMU Supercomputing Facility and TASC at TAMUQ for software support and time allocation.

# References


[1] *OpenFOAM*, OpenCFD Ltd., URL: http://openfoam.org/.

[2] J. Zweck, *How did Inmarsat deduce possible flight paths for MH370?* (2014), URL: http://www.siam.org/news/news.php?id=2151.

[3] D. Finkleman, *A mathematical and engineering approach to the search of MH370*, Powerpoint Presentation (unpublished), 2014.

[4] *Notices of the American Mathematical Society*, American Mathematical Society, URL: http://www.ams.org/notices.

[5] T. von Kármán, *The impact on seaplane floats during landing*, NACA TN 321 (1929).

[6] S. Abrate, *Hull slamming*, Applied Mechanics Reviews **64**.6 (2011), 060803.

[7] H. Wagner, *Landing of seaplanes*, NACA TM 622 (1931).

[8] A. G. Fabula, *Ellipse-fitting approximation of two-dimensional, normal symmetric impact of rigid bodies on water*, Proceedings of the 5th midwestern conference on fluid mechanics, 1957, 299–315.

[9] M Shiffman and D. Spencer, *The force of impact on a cone striking a water surface (vertical entry)*, Communications on Pure and Applied Mathematics **4**.4 (1951), 379–417.

[10] P. Garabedian, *Oblique water entry of a wedge*, Communications on Pure and Applied Mathematics **6**.2 (1953), 157–165.

[11] A. Mackey, *A mathematical model of water entry*, AUWE TN 636/79 (1979).

[12] B. Guo, P. Liu, Q. Qu, and J. Wang, *Effect of pitch angle on initial stage of a transport airplane ditching*, Chinese Journal of Aeronautics **26**.1 (2013), 17–26.

[13] G. Chen, Q. Xiong, P. J. Morris, E. G. Paterson, A. Sergeev, and Y.-C. Wang, *OpenFOAM for Computational Fluid Dynamics*, Notices of the AMS **61**.4 (2014), 354–363.

[14] C. W. Hirt and B. D. Nichols, *Volume of fluid (VOF) method for the dynamics of free boundaries*, Journal of Computational Physics **39**.1 (1981), 201–225.

[15] S. Osher and J. A. Sethian, *Fronts propagating with curvature-dependent speed: algorithms based on Hamilton-Jacobi formulations*, Journal of Computational Physics **79**.1 (1988), 12–49.

[16] M. Sussman, P. Smereka, and S. Osher, *A level set approach for computing solutions to incompressible two-phase flow*, Journal of Computational Physics **114**.1 (1994), 146–159.

[17] G. Son, *Efficient implementation of a coupled level-set and volume-of-fluid method for three-dimensional incompressible two-phase flows*, Numerical Heat Transfer: Part B: Fundamentals **43**.6 (2003), 549–565.

[18] H. Takewaki, A Nishiguchi, and T Yabe, *Cubic interpolated pseudo-particle method (CIP) for solving hyperbolic-type equations*, Journal of Computational Physics **61**.2 (1985), 261–268.

[19] G. Wu, H Sun, and Y. He, *Numerical simulation and experimental study of water entry of a wedge in free fall motion*, Journal of Fluids and Structures **19**.3 (2004), 277–289.

[20] T. Wierzbicki and D. K. Yue, *Impact damage of the Challenger crew compartment*, Journal of Spacecraft and Rockets **23**.6 (1986), 646–654.

[21] T. Wierzbicki and D. Yue, *Spacecraft crashworthiness - Towards reconstruction of the Challenger accident*, American Society of Mechanical Engineers, Applied Mechanics Division, AMD **79** (1986), 31–46.

[22] E. L. Fasanella, E Widmayer, and M. P. Robinson, *Structural analysis of the controlled impact demonstration of a jet transport airplane*, Journal of Aircraft **24**.4 (1987), 274–280.

[23] J. R. McGehee, M. E. Hathaway, and V. L. Vaughan, *Water-landing characteristics of a reentry capsule*, National Aeronautics and Space Administration, 1959.

[24] F. Liu, Q. Qu, B. Guo, X. Jin, J. Wu, and K. Zhang, *Application of computational fluid dynamics in the planned ditching of a transport airplane*, Mechanics and Practices **36** (2014), (in Chinese with English abstract), 278–284.

[25] *Abaqus FEA*, Dassault Systèmes Simulia Corp., URL: `http://www.3ds.com/products-services/simulia`.

[26] *LS-DYNA*, Livermore Software Technology Corp., URL: `http://www.lstc.com/products/ls-dyna`.

[27] A. Barnett, *Cross-national differences in aviation safety records*, Transportation science **44**.3 (2010), 322–332.

# Structural Failure of Aircraft Fuselage in Water Entry

Cong Gu, Goong Chen, and Tomasz Wierzbicki

# Hydrodynamic Computation and Examples

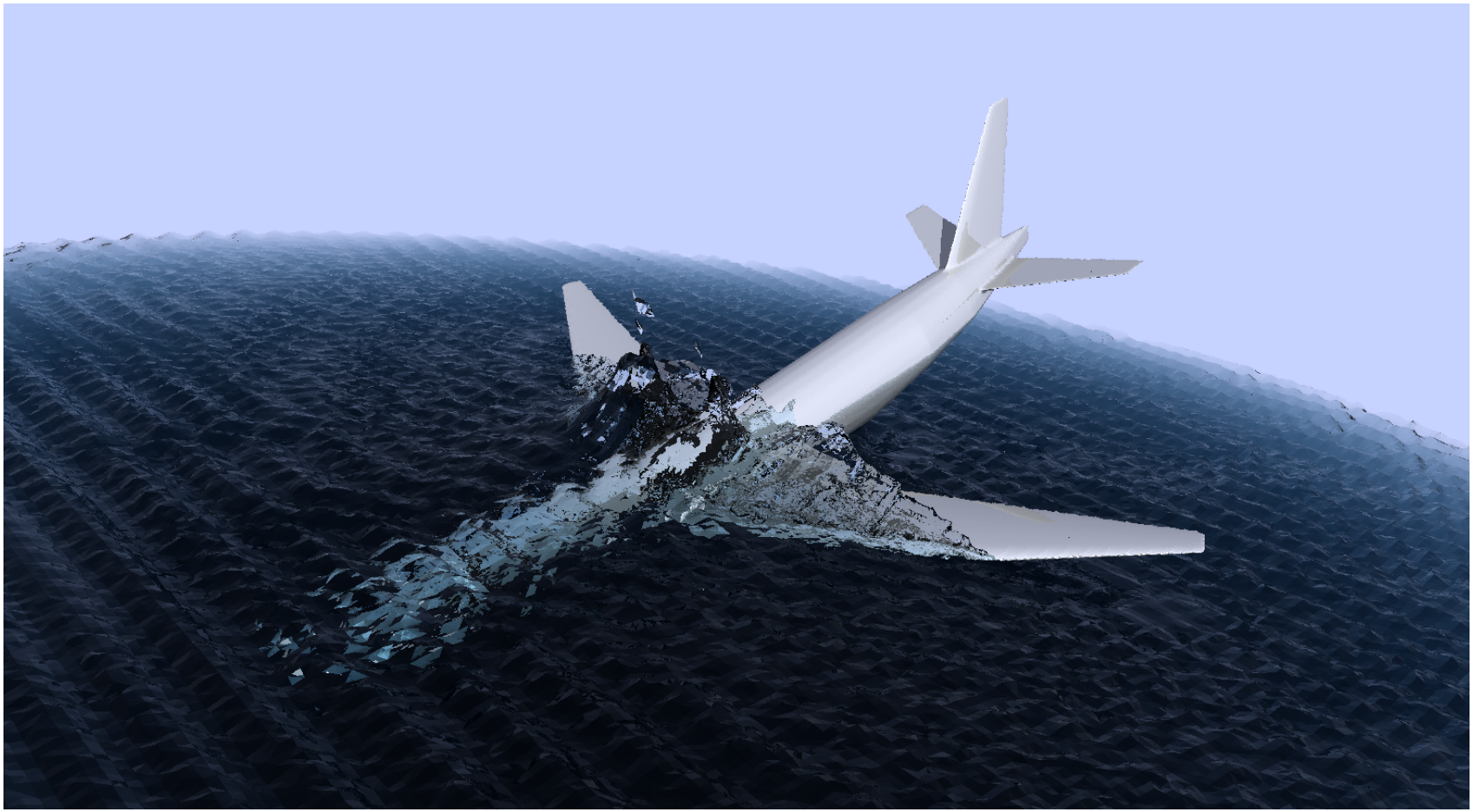

# Hydrodynamic Computation and Examples

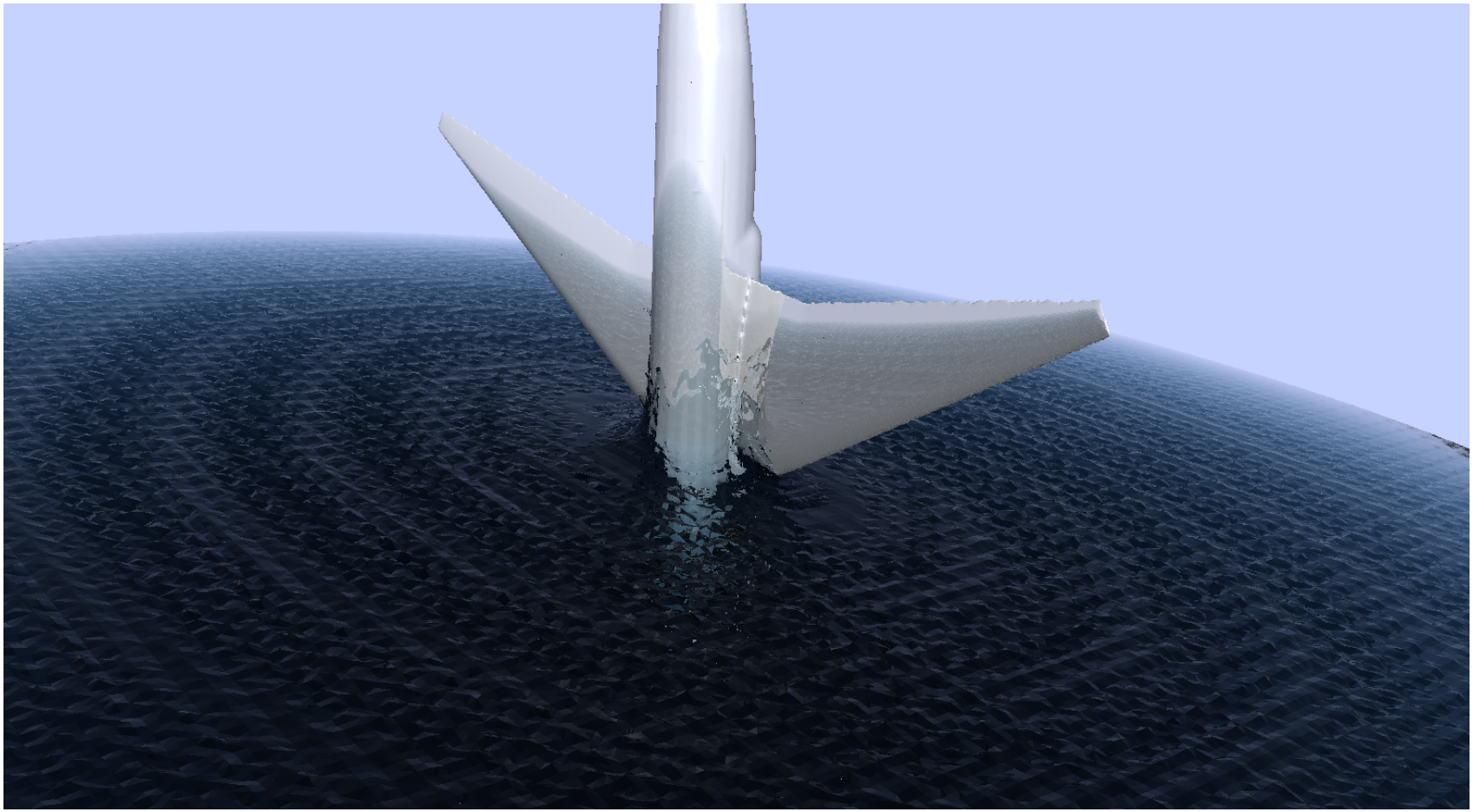

# Introduction

In [1], water entry process of an aircraft is simulated using CFD techniques. The aircraft is assumed to be a rigid body with free motion in a mixture of air and water. The current study aims to answer the question whether the aircraft can survive the water entry process described in the simulation.
Ideally, a couple fluid-structural interaction simulation is required to fully understand the process. However, such a simulation, especially involving rapid fracture and disintegration can be quite challenging. The strategy employed here is an uncoupled structural analysis. Data are obtained from CFD simulation to serve as external load in the structural analysis. Some choices made here. A full-blown 3D analysis is avoided in this study, since such an analysis would require a more detailed description of the aircraft structure to be useful. Analysis based on rigid beam theory is used here as a simplified model. To this end, beam theory will be described and applied to the fuselage of the aircraft in the following.

# Free-Free Rigid Beam I

Dynamic failure of free-free beam was studied in [2, 3]. Plastic failure is predicted when the bending moment developed in the beam exceeds a critical value. Here, the fuselage of the aircraft is described as a rigid beam. It takes into account the bending moment, lateral displacement and rotary inertia, but not deformation of any kind. The governing equations are, for $x \in [0, L]$,

$$\begin{aligned} \frac{\partial V}{\partial x} + q_z &= \lambda a_z, \\ \frac{\partial N}{\partial x} + q_x &= \lambda a_x, \\ \frac{\partial M}{\partial x} - V + \tau &= \eta\alpha, \end{aligned}$$

Free-free boundary condition, namely zero forcing at both ends, is used as

$$M(0) = M(L) = 0, \qquad N(0) = N(L) = 0, \qquad V(0) = V(L) = 0.$$

# Free-Free Rigid Beam II

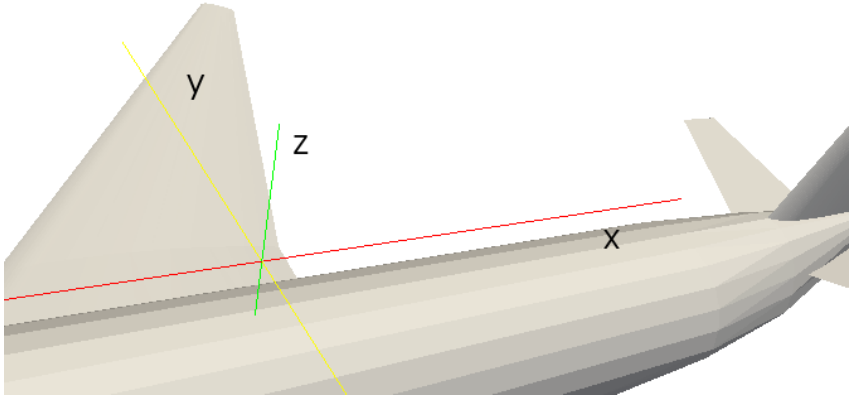


Figure 1: Direction of axes.

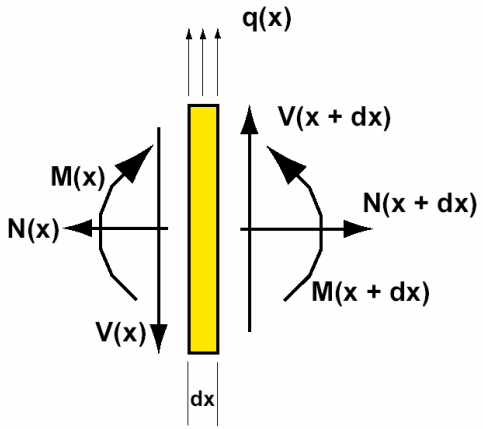


Figure 2: Beam element subject to forces and moments.

# Free-Free Rigid Beam III

$(x, y, z)$ are body-local axes for roll, pitch and yaw respectively (see Figure 1), $q_z$ and $q_x$ (N/m) are external force in $z$ and $x$ direction per unit length, $\tau$ (N·m/m) is external pure torque in $y$ direction per unit length measured at the center of cross section, $V$ (N) is internal shear force, $M$ (N·m) is internal bending moment, $N$ (N) is internal axial ($x$) force, $\eta$ (kg·m) is sectional moment of inertia in $y$ direction measured at the neutral position, $\lambda$ (kg/m) is linear mass density, $a_z$ and $a_x$ (m/sec$^2$) are the acceleration in $z$ and $x$ direction respectively, and $\alpha$ (1/sec$^2$) is the angular acceleration in $y$ direction. See Figure 2 for an illustration of a beam element. All other motion are ignored.

# Global Motion I

Since CFD data is available only at certain snapshots in time, acceleration terms in the equation have to be evaluated using information from the current time instance only. This is also essential for satisfaction of boundary condition at both ends simoutaneously, which will be shown in when the equations are integrated.
In general, neutral positions of cross sections should be given. But for estimation purposes, they are aligned to a line parallel to $x$-axis (ignored). The instantaneous global motion is described by the following rigid body dynamics,

# Global Motion II

$$m = \int_0^L \lambda(x_1)\, dx_1, \qquad F_x = \int_0^L q_x(x_1)\, dx_1, \qquad F_z = \int_0^L q_z(x_1)\, dx_1,$$

$$T = \int_0^L \Big[\tau(x_1) - q_z(x_1)(x_1 - x_0)\Big]\, dx_1,$$

$$J = \int_0^L \Big[\lambda(x_1)(x_1 - x_0)^2 + \eta(x_1)\Big]\, dx_1,$$

$$\alpha = T/J,$$

$$a_x(x) = -\omega^2(x - x_0) + F_x/m, \qquad a_z(x) = -\alpha(x - x_0) + F_z/m,$$

where $\omega$ is the angular velocity (1/sec) in $y$ direction.

# Data Processing I

Values needed for the above calculation are $q_z$, $q_x$, $\tau$, $\lambda$, $\eta$ and $\omega$. Angular velocity $\omega$ is directly read from the simulation, since it won't interfere with boundary condition. Other Data input from CFD are the aircraft geometry and the external stress $\boldsymbol{\sigma}$ on the aircraft surface at each snapshot in time. Figure 3 shows an example of instant pressure distribution on the geometry.

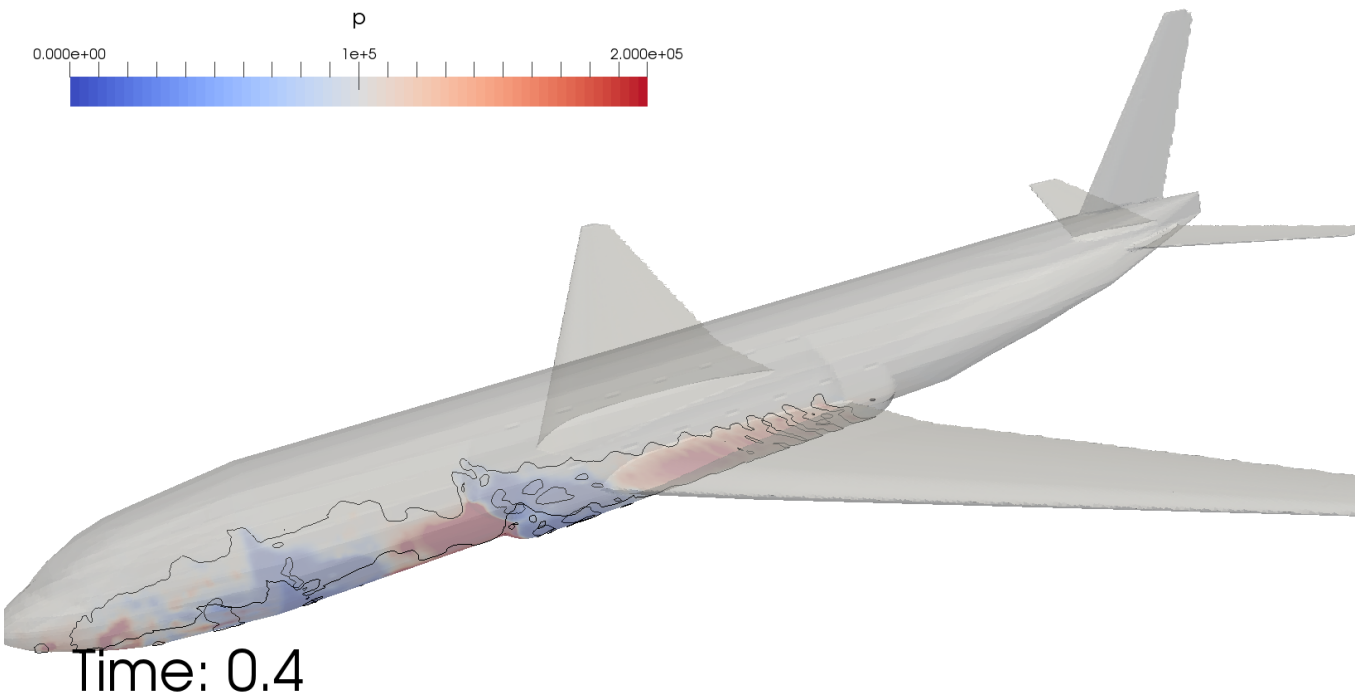


Figure 3: Pressure distribution on aircraft surface. Black line is the three-phase contact line.

# Data Processing II

To perform a numerical beam analysis along the $x$-axis, the aircraft surface is partitioned, equally in $x$-axis, into $n$ segments $S_j$, $j = 1, 2, ..., n$. Figure 4 shows an example of partitioning into 100 segments. Piecewise constant values are assumed for numerical caluculation.

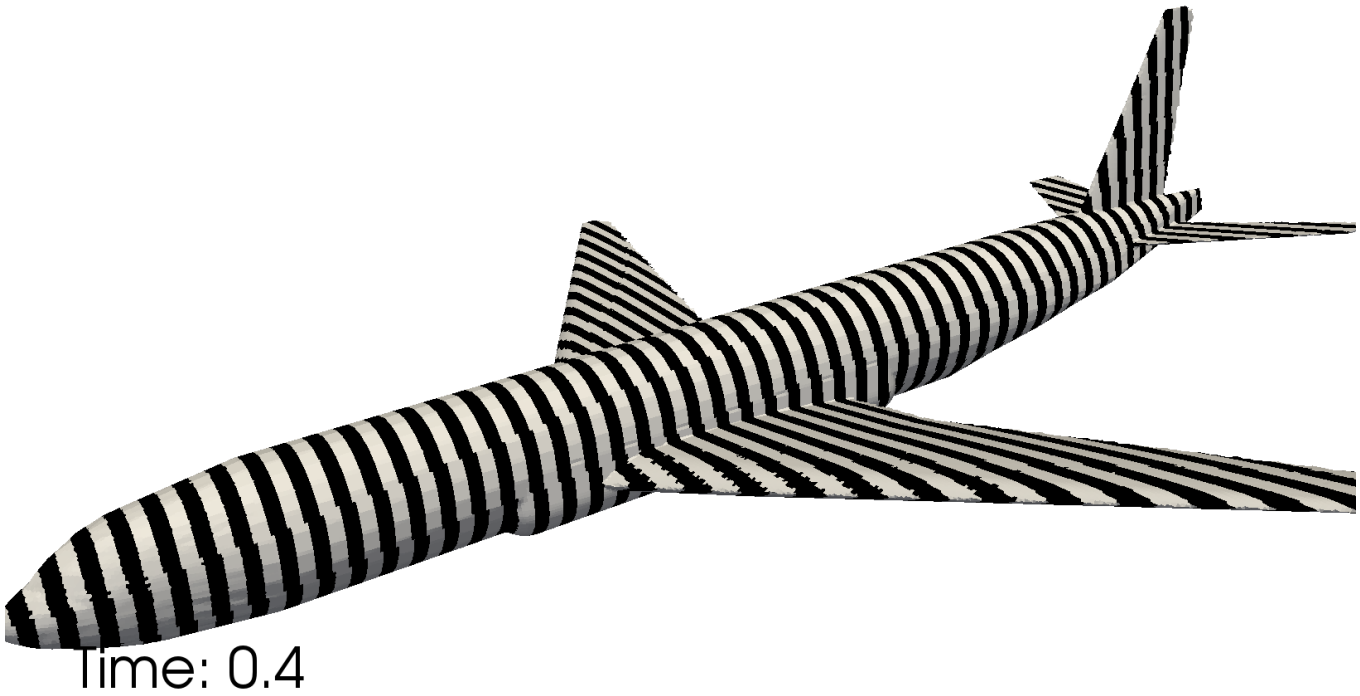


Figure 4: Partition of the aircraft surface along the $x$-axis. Number of segments $n = 100$.

# Data Processing III

First, the center in $z$ direction is calculated by

$$z_j = \frac{1}{|S_j|} \int_{S_j} z \, dS.$$

This $z_j$ serves as the neutral position. Values of $z_j$ are shown in Figure 5. The distribution of mass and rotary inertia are calculated also using the available geometry. Since detailed interior model of the aircraft is not available, for simplicity, we assume mass is distributed to each segment proportional to the surface area $|S_j|$.

$$\lambda_j = \frac{c}{l} |S_j| ,$$

where $l = L/n$, and coefficient $c$ (kg/m$^2$) is determined by matching a given total mass of the aircraft. As for the sectional moment of inertia, we assume half of the mass is uniformly distributed on the surface, and the other half is located near the neutral position, thus does not have much contribution,

$$\eta_j = \frac{c}{2l} \int_{S_j} (z - z_j)^2 \, dS.$$

Values of $\lambda$ and $\eta$ are shown in Figure 6 and 7

# Data Processing IV

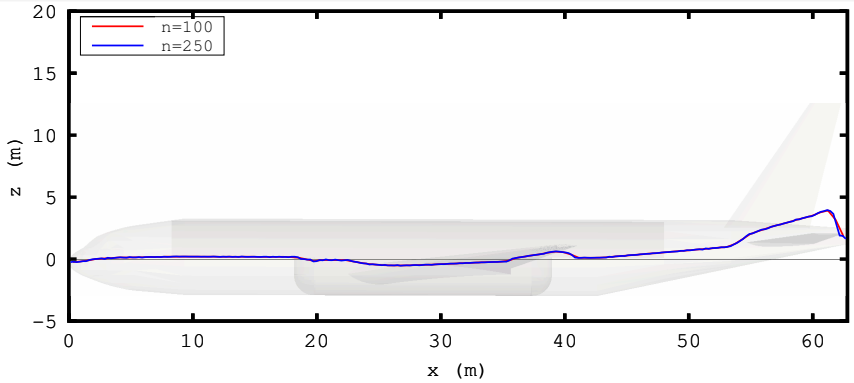


Figure 5: Center in $z$ direction along the aircraft body.

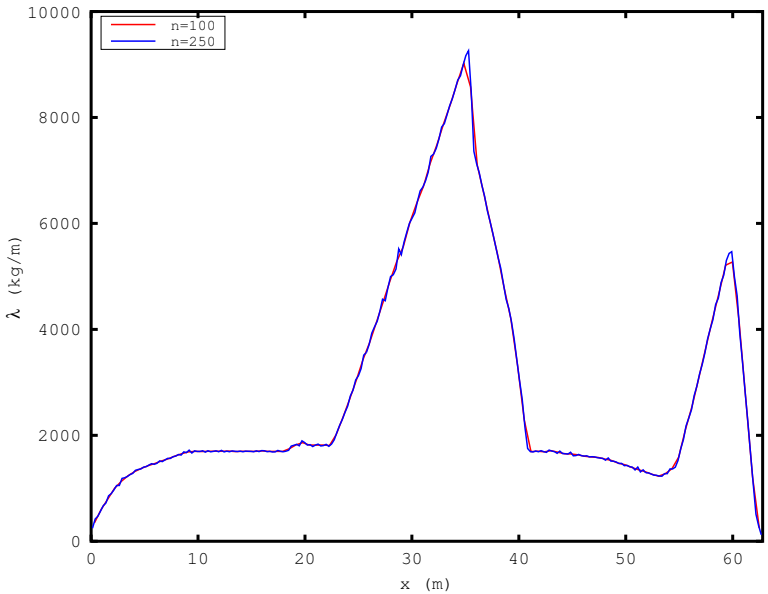


Figure 6: Distribution of mass $\lambda$ along the aircraft body.

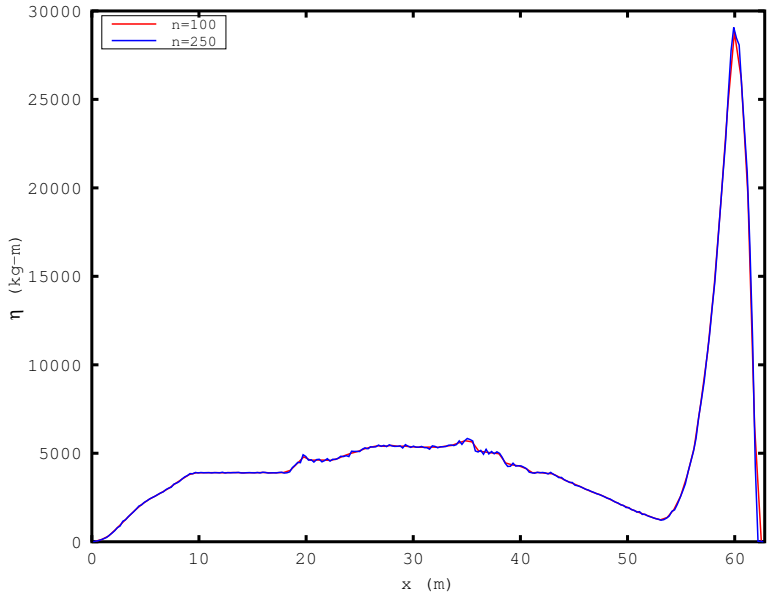


Figure 7: Distribution of rotary inertia $\eta$ along the aircraft body.

# Data Processing V

It is assumed that there is a pressure of $p_0$ in the cabin, therefore, the external load on the beam is calculated as

$$\boldsymbol{q}_j = \frac{1}{l}\int_{S_j} (\boldsymbol{\sigma} - p_0\boldsymbol{I})\hat{\boldsymbol{n}}\, dS, \qquad \tau_j = \frac{1}{l}\int_{S_j} (z - z_j)\hat{\boldsymbol{k}} \times (\boldsymbol{\sigma} - p_0\boldsymbol{I})\hat{\boldsymbol{n}}\, dS.$$

$\boldsymbol{q}_j$ is then projected to $x$ and $z$ directions as $q_{x,j}$ and $q_{z,j}$ respectively. Figures 8–10 show the distributions of external force load $q_x$, $q_z$ and torque $\tau$ for the example given in Figure 3. Data is smoothed out a little and peak values are reduced if there is a smaller number of segments $n$. Relative magnitude and direction of the load along aircraft body is illustrated in Figure 11, to be compared with Figure 3.

# Data Processing VI

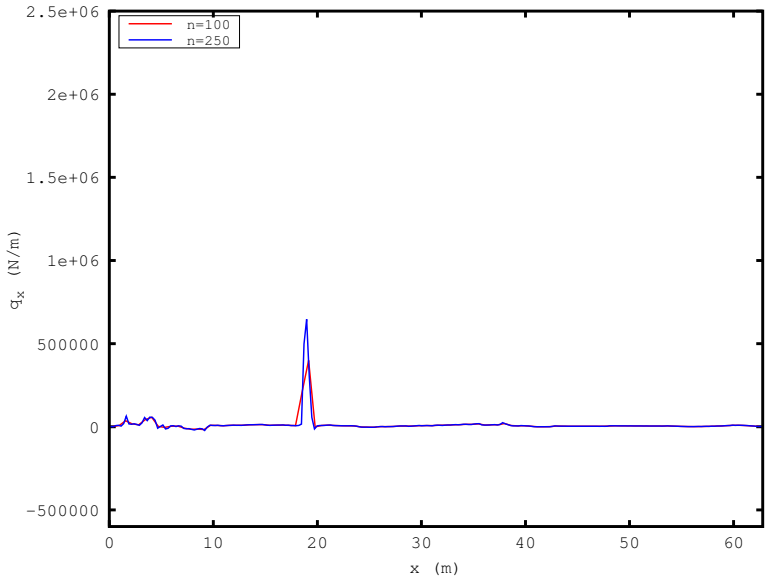


Figure 8: Distribution of external load $q_x$ along the aircraft body for the example given in Figure 3.

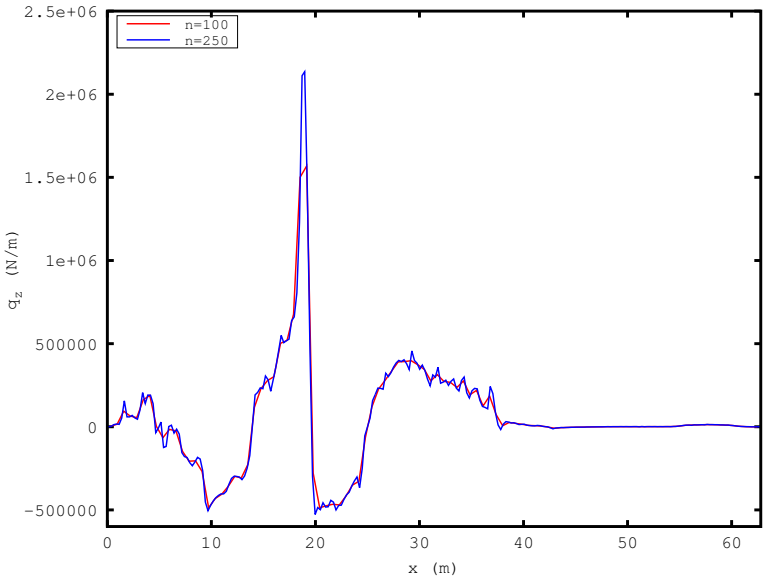


Figure 9: Distribution of external load $q_z$ along the aircraft body for the example given in Figure 3.

# Data Processing VII

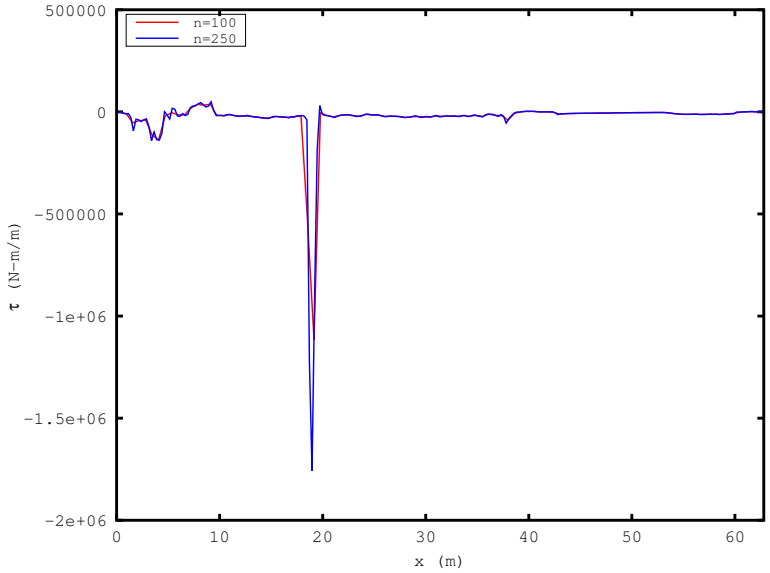


Figure 10: Distribution of external pure torque $\tau$ along the aircraft body for the example given in Figure 3.

# Data Processing VIII

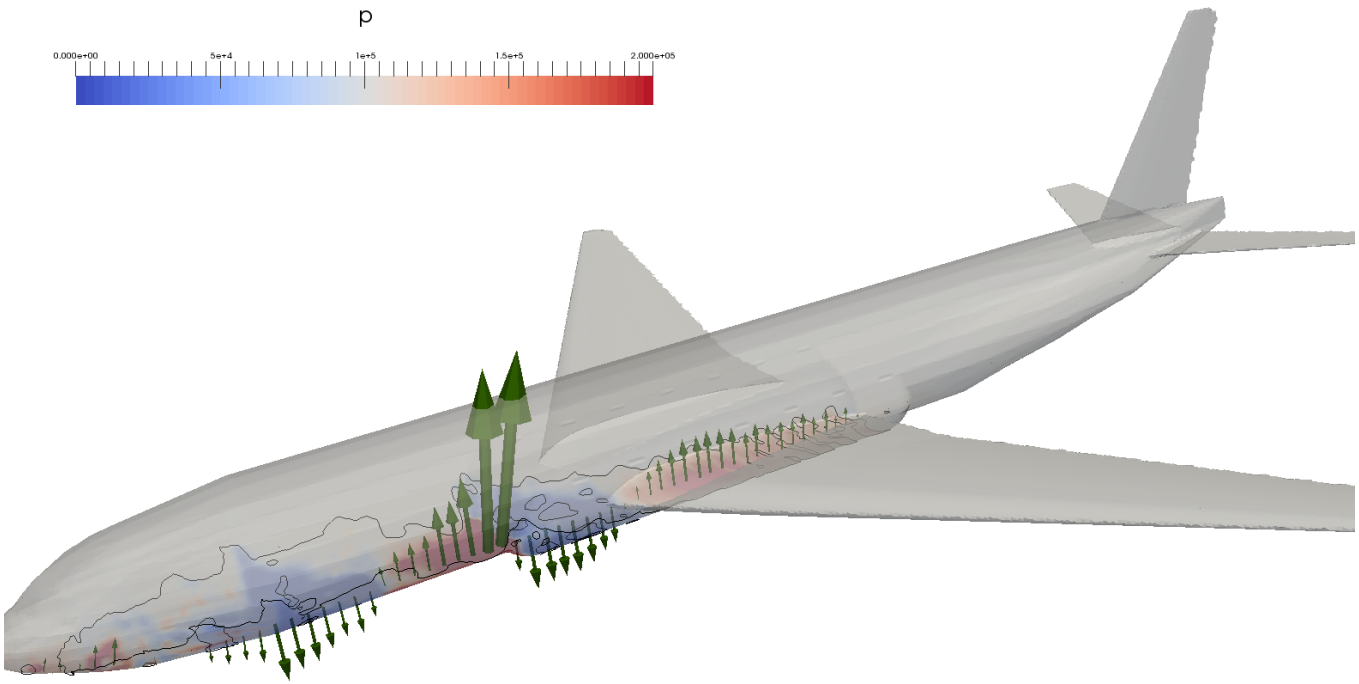


Figure 11: Relative magnitude and direction of the external load obtained in data processing is added as vector arrows to Figure 3.

Note that the vertical center $z_j$ is only considered in this subsection. As mentioned previously, neutral positions are artificially aligned to a line parallel to $x$-axis in order to simplify calculation.

# Direct Integration of the Beam Equations I

Integration of the beam equations with boundary condition at $x = 0$ gives

$$V(x) = \int_0^x \Big[ -q_z(x_1) + \lambda(x_1) a_z(x_1) \Big] \, dx_1$$

$$N(x) = \int_0^x \Big[ -q_x(x_1) + \lambda(x_1) a_x(x_1) \Big] \, dx_1$$

$$M(x) = \int_0^x \Big[ V(x_1) - \tau(x_1) + \alpha\eta(x_1) \Big] \, dx_1.$$

The problem is to make sure the boundary condition is also satisfied at the other end $x = L$. In fact, by direct calculation as in Appendix, it is automatically satisfied. Figures 12-14 show the strength of internal forces and bending moment for the example given in Figure 3. The comparison between $n = 100$ and $n = 250$ reveals that results do not depend much on the choice of $n$ if $n$ is as large as $100$.

# Direct Integration of the Beam Equations II

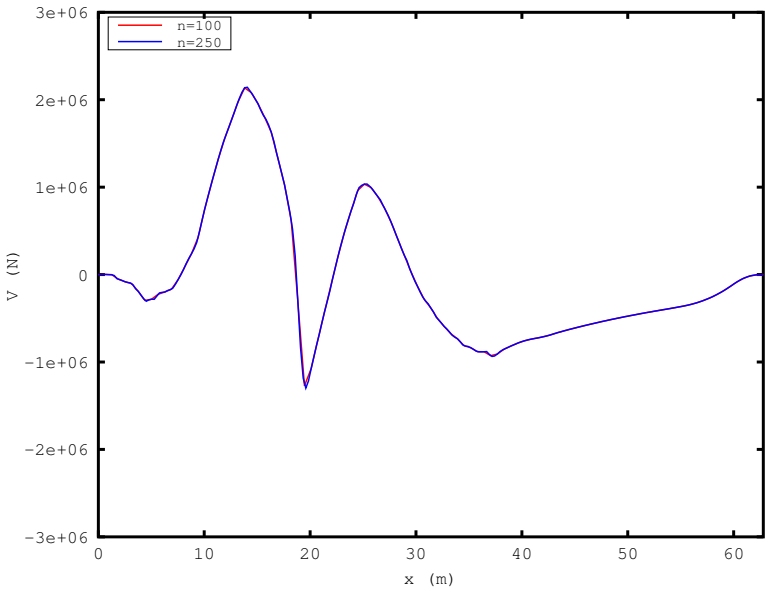


Figure 12: Internal shear force $V$ along aircraft body.

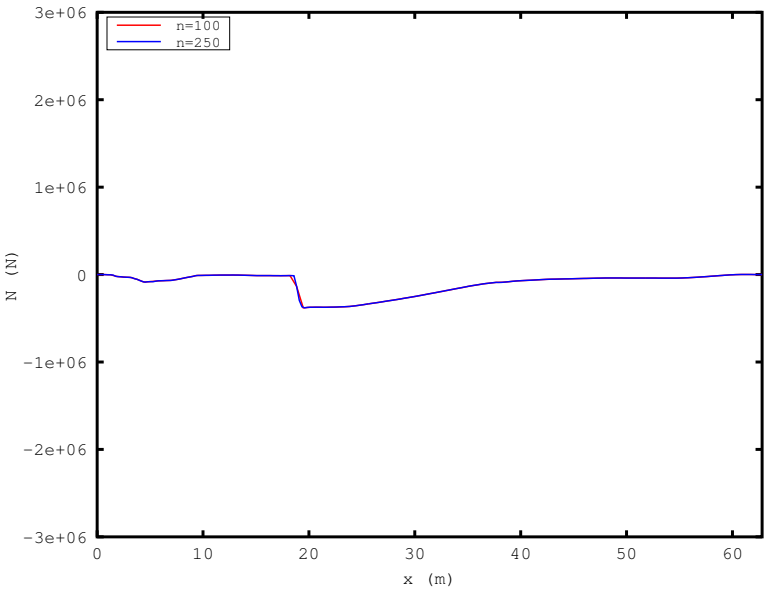


Figure 13: Internal axial force $N$ along aircraft body.

# Direct Integration of the Beam Equations III

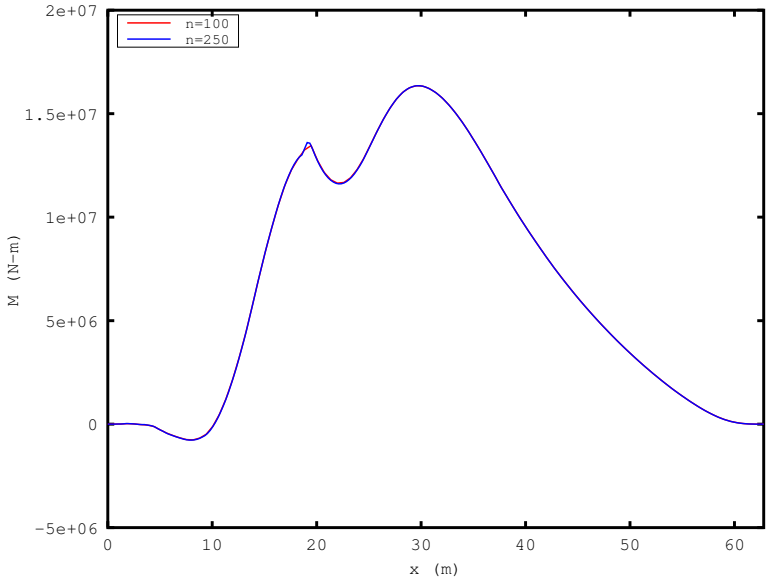


Figure 14: Internal bending moment $M$ along aircraft body

# Bending of Cylindrical Shell I

Buckling caused by excessive compressive stress is considered here. As proposed in [4], critical compressive stress for a cylindrical shell before buckling failure is given by

$$\sigma_{\text{cr}} = \frac{Et_{\text{eq}}}{R\sqrt{3(1-\nu^2)}},$$

where $E$ is the Young's modulus, $t_{\text{eq}}$ is shell wall thickness, $R$ is radius of the cylinder and $\nu$ is Poisson's ratio. The maximum compressive stress induced by $M$ and $N$ is given by

$$\sigma_{\text{max}} = \frac{M}{\pi R^2 t_{\text{eq}}} - \frac{N}{2\pi R t_{\text{eq}}}.$$

Therefore, we compare the effective bending moment

$$M' = M - NR/2,$$

with critical value

$$M_{\text{cr}} = \frac{\pi E R t_{\text{eq}}^2}{\sqrt{3(1-\nu^2)}},$$

This is regarded as a good estimation for short cylinders. Using values from Table 1, we get $M_{\text{cr}} = 4.35 \times 10^7$ N·m.

# Bending of Cylindrical Shell II

| | |
|---|---|
| Geometry | |
| Radius of cylinder | $R = 3.1$ m |
| Equivalent thickness | $t_{eq} = 1$ cm (?) |
| Material (Aluminum 2024-T351) | |
| Poisson's ratio | $\nu = 0.33$ |
| Young's modulus | $E = 73.1$ GPa |

Table 1: Parameters for critical bending moment calculation.

# Bending of Cylindrical Shell III

Now we find the maximum of effective bending moment $M'$ over the whole fuselage for each time snapshot $t$, getting $M'_{\text{max}}(t)$. They are then plotted versus $t$ in Figures 15–18 in comparison with the critical bending moment $M_{\text{cr}}$. Here are some interpretations for those four scenarios.

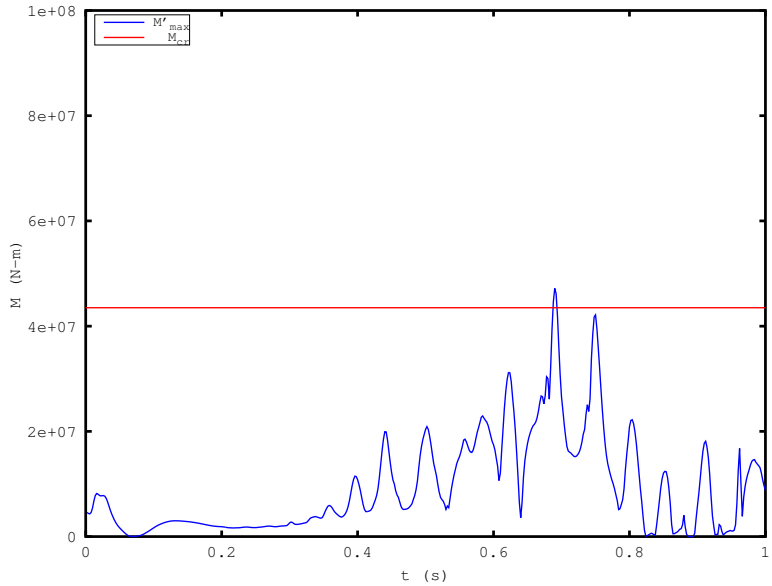


Figure 15: Maximum effective bending moment $M'_{\text{max}}$ for the scenario with $8^\circ$ pitch angle.

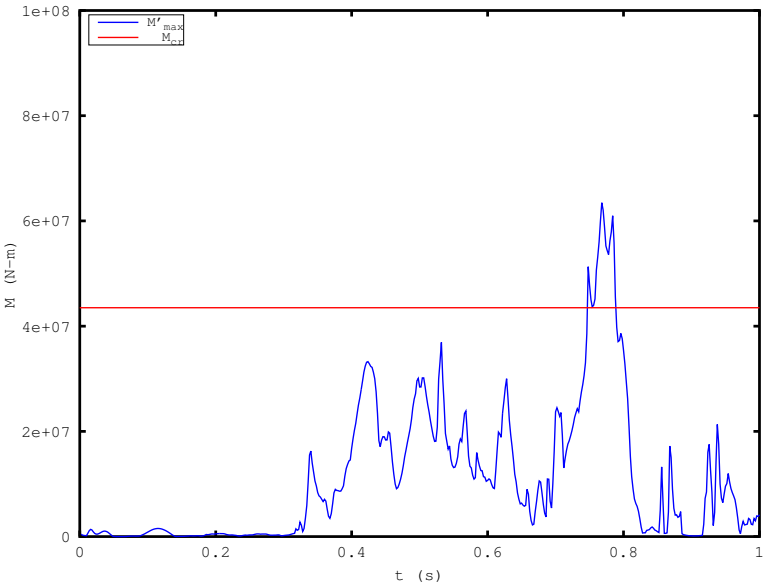


Figure 16: Maximum effective bending moment $M'_{\text{max}}$ for the scenario with $-3^\circ$ pitch angle.

# Bending of Cylindrical Shell IV

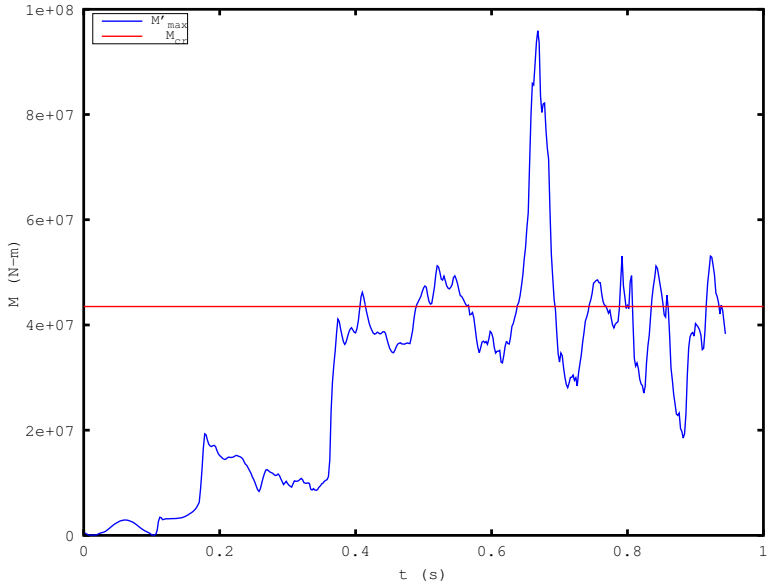


Figure 17: Maximum effective bending moment $M'_{\text{max}}$ for the scenario with $-30^\circ$ pitch angle.

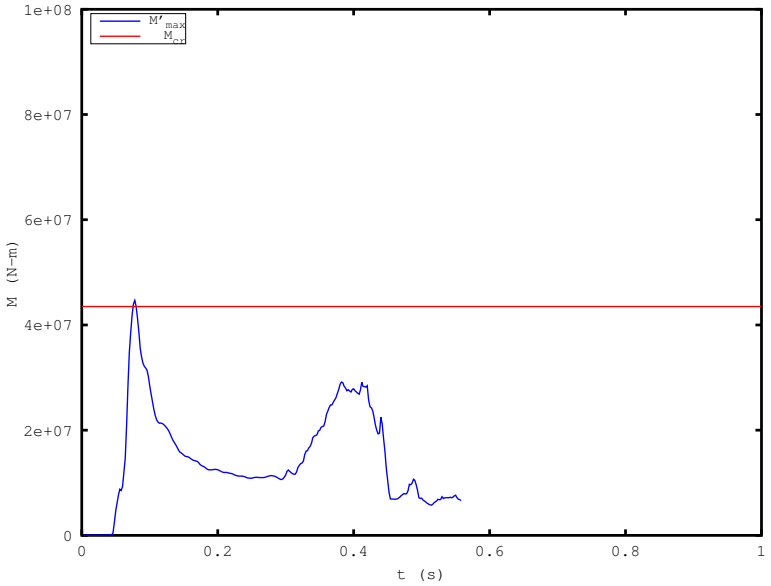


Figure 18: Maximum effective bending moment $M'_{\text{max}}$ for the scenario with $-90^\circ$ pitch angle.

# Bending of Cylindrical Shell V

- Scenario with $8^\circ$ pitch angle (Figure 15). Plane is generally safe from structural failure. The process is also known as ditching. Large temoprary bending moment can be observed if ditching on a wavy sea and when the speed of the aircraft is still high, for example, at around $t = 0.7$ s. See Figure 19.
- Scenario with $-3^\circ$ pitch angle (Figure 16). The plane might recover to the ditching posture. However, it have to overcome a period of large bending moment when the middle or tail parts of the fuselage hit water, for example, at around $t = 0.78$ s. See Figure 20.
- Scenario with $-30^\circ$ pitch angle (Figure 17). The plane is subject to large axial compression and asymmetric external load, for example, starting from $t = 0.4$ s. Therefore the aircraft is most likely to suffer global failure. See Figure 21.
- Scenario with $-90^\circ$ pitch angle (Figure 18). The plane is subject to axial compression, but not much bending due to the symmetric external load. This lasts until wings reach the water, which is not simulated. See Figure 22.

# Bending of Cylindrical Shell VI

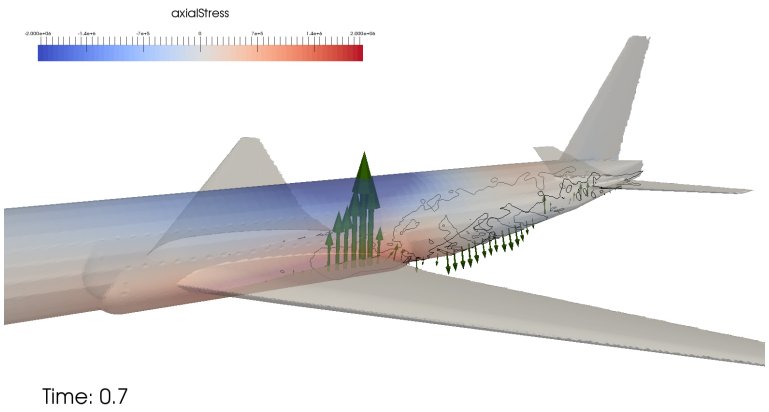


Figure 19: External load and axial stress for the scenario with $8^\circ$ pitch angle at $t = 0.7$ s.

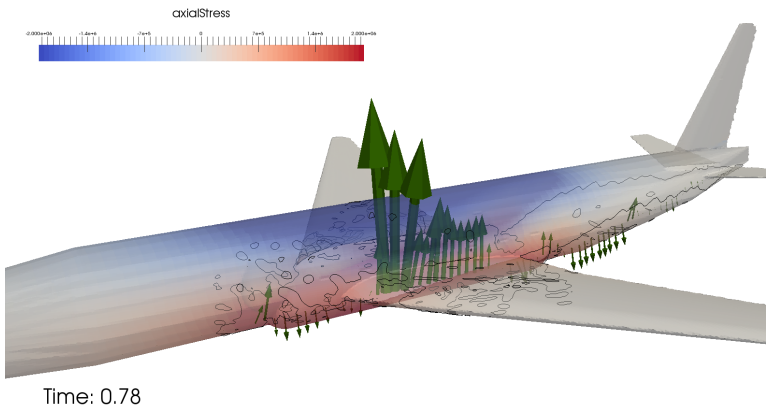


Figure 20: External load and axial stress for the scenario with $-3^\circ$ pitch angle at $t = 0.78$ s.

# Bending of Cylindrical Shell VII

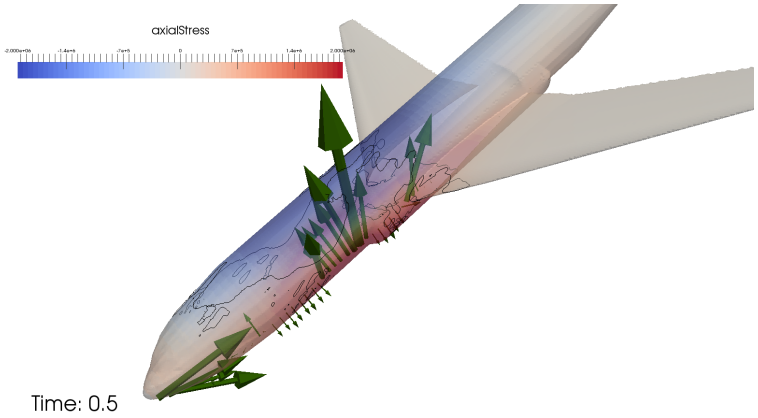


Figure 21: External load and axial stress for the scenario with $-30^\circ$ pitch angle at $t = 0.5$ s.

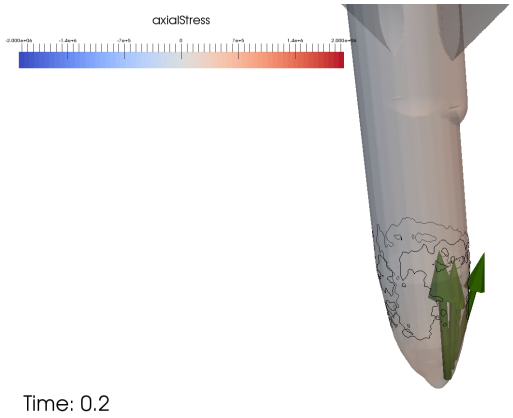


Figure 22: External load and axial stress for the scenario with $-90^\circ$ pitch angle at $t = 0.2$ s.

# Other Failure Modes

Tearing, shear, stringers, rings, etc.

# Appendix: Boundary Condition at $x = L$

$$
\begin{aligned}
&M(L)\\
&= \int_0^L V(x_2)\,dx_2 - \int_0^L \tau(x_1)\,dx_1 + \alpha \int_0^L \eta(x_1)\,dx_1\\
&= \int_0^L \int_0^{x_2} \Big[ - q_z(x_1) + \lambda(x_1) a_z(x_1) \Big]\,dx_1\,dx_2 - \int_0^L \tau(x_1)\,dx_1 + \alpha \int_0^L \eta(x_1)\,dx_1\\
&= \int_0^L \Big[(L - x_0) - (x_1 - x_0)\Big] \Big[ - q_z(x_1) + \lambda(x_1) a_z(x_1) \Big]\,dx_1 - \int_0^L \tau(x_1)\,dx_1 + \alpha \int_0^L \eta(x_1)\,dx_1\\
&= (L - x_0) \int_0^L \Big[ - q_z(x_1) + \lambda(x_1) \Big( - \alpha(x_1 - x_0) + F_z/m \Big) \Big]\,dx_1\\
&\quad - \int_0^L (x_1 - x_0) \Big[ - q_z(x_1) + \lambda(x_1) \Big( - \alpha(x_1 - x_0) + F_z/m \Big) \Big]\,dx_1 - \int_0^L \tau(x_1)\,dx_1 + \alpha \int_0^L \eta(x_1)\,dx_1\\
&= (L - x_0) \left[ - \int_0^L q_z(x_1)\,dx_1 - \alpha \int_0^L \lambda(x_1)(x_1 - x_0)\,dx_1 + (F_z/m) \int_0^L \lambda(x_1)\,dx_1 \right]\\
&\quad - \int_0^L \Big[ \tau(x_1) - q_z(x_1)(x_1 - x_0) \Big]\,dx_1 + \alpha \int_0^L \Big[ \lambda(x_1)(x_1 - x_0)^2 + \eta(x_1) \Big]\,dx_1\\
&\quad - (F_z/m) \cdot \int_0^L \lambda(x_1)(x_1 - x_0)\,dx_1\\
&= (L - x_0) \Big[ - F_z - 0 + (F_z/m) \cdot m \Big] - T + \alpha J - 0\\
&= 0
\end{aligned}
$$


G. Chen, C. Gu, P. J. Morris, E. G. Paterson, A. Sergeev, Y.-C. Wang, and T. Wierzbicki. "Malaysia airlines flight MH370: water entry of an airliner". In: *Notices of the AMS* 62.4 (2015), pp. 330–344.


N. Jones and T. Wierzbicki. "Dynamic plastic failure of a free-free beam". In: *International Journal of Impact Engineering* 6.3 (1987), pp. 225–240.


J. Yang, T. Yu, and S. Reid. "Dynamic behaviour of a rigid, perfectly plastic free–free beam subjected to step-loading at any cross-section along its span". In: *International journal of impact engineering* 21.3 (1998), pp. 165–175.


S. Timoshenko and J. M. Gere. *Theory of elasticity stability*. McGraw, 1961.